THESIS FOR THE DEGREE OF LICENTIATE OF ENGINEERING

Intermodulation Distortion in Active and Passive Components

Martin Mattsson

CHALMERS
UNIVERSITY OF TECHNOLOGY

Department of Microtechnology and Nanoscience - MC2
Chalmers University of Technology
Gothenburg, Sweden, 2023

Intermodulation Distortion in Active and Passive Components

Martin Mattsson

© Martin Mattsson 2023

Chalmers University of Technology
Department of Microtechnology and Nanoscience - MC2
Microwave Electronics Laboratory
SE-412 96 Gothenburg, Sweden
Phone: +46 (0)31 772 1000

ISSN 1652-0769
Technical Report No. MC2-464

Printed by Chalmers Reproservice
Gothenburg, Sweden, May 2023

Till Sofie och Tage

Abstract

Wireless communication is growing rapidly, and the demand for higher data rate, low latency, and availability leads to a more complex infrastructure with new challenges. Multiple communication systems have to co-exist in a densely populated frequency-spectrum, where higher power levels and more sensitive receivers are required. However, this also increases the potential risk of interference from weakly spurious signals that are detectable by these sensitive receivers, leading to a degradation in the performance of the communication systems. The unwanted spurious signals are generated when two or more signals of different frequencies pass through a nonlinear element, resulting in mixing products. If the mixing products are produced in an active device, they are referred to as intermodulation distortion (IMD). In passive devices, they are referred to as passive intermodulation (PIM) distortion. The requirements for highly linear devices are increasing because of these new challenges. Therefore, a better understanding of the nonlinear behavior is imperative to develop accurate nonlinear models that will aid in mitigating IMD.

This thesis analyze and model IMD in periodic structures. The periodic structure employed in this thesis is a loaded-line phase shifter that is periodically loaded by varactor-diodes, which are highly nonlinear elements that generate IMD in the forward and backward direction. In a multi-source environment, the IMD from each source creates a interference pattern that can add constructively or destructively. The IMD generated in loaded-line phase shifters have been investigated for several design factors, e.g., periodicity, bias condition, input power, number of unit cells, and capacitance per unit cell length. Moreover, it was demonstrated that the capacitance-voltage relationship in a hyperabrupt varactor-diode has to be accurately modeled to predict the sensitive nonlinear behavior. A polynomial varactor model was employed and experimentally validated with satisfactory results. The model was scaled and evaluated further in a circuit simulator to investigate if there is an optimum design of loaded-line phase shifters in terms of phase-shift/loss and linearity. It was demonstrated that evenly distributing the varactor capacitance for the same varactor capacitance per unit length improves the phase shift/loss. Additionally, it showed that there is a trade-off between low loss and low IMD.

Keywords: Intermodulation distortion, passive intermodulation, loaded-line phase shifter, varactor modeling, hyperabrupt junction, nonlinear analysis, polynomial model

List of publications

The following appended papers constitute the main work for this thesis:

Paper A **M. Mattsson** and D. Kuylenstierna, "Multi-source Intermodulation in a Loaded-line Phase Shifter," in *2020 50th European Microwave Conference (EuMC),* Utrecht, Netherlands, 2021, pp. 280-283.

Paper B **M. Mattsson** and D. Kuylenstierna, "Experimental Investigation of Distributed Intermodulation in an Artificial Transmission Line," in *Multipactor, Corona and Passive Intermodulation (MULCOPIM),* Valencia, Spain, 2022.

Paper C **M. Mattsson**, K. Buisman and D. Kuylenstierna, "Modeling of Intermodulation in a Loaded-line Phase Shifter Based on a Polynomial Varactor Model," submitted to *IEEE Transactions on Microwave Theory and Techniques,* 2023.

Acknowledgments

First of all, I would like to express my sincere gratitude to my main supervisor, Dan Kuylenstierna, for the invaluable guidance and support throughout this journey. I am deeply grateful for your encouragement, kindness, and technical discussions, which have enriched my understanding and skills. Your availability and willingness to provide fast and insightful feedback have been a great asset, and I feel very privileged to have you as a supervisor.

I would like to extend my sincere gratitude to Koen Buisman, my co-supervisor, for the support and our technical discussions about modeling and measurements. Your insightful advice has been pivotal in shaping the outcome of this project. It is a great pleasure to have you as a co-supervisor, and even though you don't live in Sweden, your availability and responsiveness have been exceptional. You have the fastest email response known to mankind.

I would like to thank Joakim Johansson and Richard Udiljak from Beyond Gravity for their support and interesting technical discussions.

I want to thank everyone at the Microwave Electronics Laboratory for creating a great working environment, and where I have met many new friends for life. A special thanks goes to Frida, Han, Vessen, Oli, Hassona, Decha, Jonas, and Juan. Thank you for all the good times, and making the work environment to something else than only work. You have made this experience so much more enjoyable.

I want to thank all my friends in Stockholm, which I miss dearly, for all the great experiences I have had with you through my life, and you always bring so much happiness to me. Also, thanks to my wonderful mom, dad, and brothers, who I can always rely on and give me all the support there is. I am lucky to have you.

Lastly, but most importantly, I want to express my deepest appreciation to Sofie, and our son Tage. I couldn't have accomplished this without you. You two make my day, every day, and helped me appreciate what truly matters in life. Thank you Sofie for always being there for me and for your unconditional love. I am forever grateful for everything you have done for me. I love you!

Notations and abbreviations

Notations

$\bar{B}$	Normalized load susceptance
C_0	Load capacitance of loaded transmission line
C_j	Variable junction capacitance
C_{j0}	Zero bias junction capacitance
C_n	Polynomial coefficient of the n^{th}-order
C_p	Parallel capacitance in varactor model
C_t	Shunt capacitance per unit cell length
C_v	Thermal capacity at constant volume
C_V	Varactor-diode capacitance
c_0	Speed of light in vacuum
d	Period of periodic structure
f	Frequency
f_B	Bragg frequency
$F_{\Delta\phi}$	Phase shifter figure of merit [deg./dB]
J	Current density
L_s	Series inductance in varactor model
L_{dB}	Loss in dB
n	Grading coefficient in diode
R_{th}	Thermal resistance
R_s	Series resistance in varactor model
T	Temperature
V_R	Reversed bias voltage
Z_0	Unloaded transmission line impedance
Z_e	Effective characteristic impedance of loaded transmission line
β	Phase constant in loaded line phase shifter
$\Delta\phi$	Differential phase shift
ϵ_r	Relative electric permittivity
ϕ	Built-in potential in diode
ρ_{e0}	Static resistivity
θ_0	Electrical length of unloaded transmission line
θ_e	Effective electrical length of loaded transmission line
ω	Angular frequency

Abbreviations

ADS:	Advanced Design System
AESA:	Active Electronically Ateerable Arrays
CPWG:	Grounded Coplanar Waveguide
DC:	Direct Current
DUT:	Device Under Test
FDTD:	Finite-difference in Time-domain
FOM:	Figure Of Merit
FTT:	Fast Fourier-Transform
HD_2:	Second-order Harmonic Distortion
HD_3:	Third-order Harmonic Distortion
IL:	Insertion Loss
IM:	Intermodulation
IM_2:	Second-order Intermodulation Distortion
IM_3:	Third-order Intermodulation Distortion
IM_5:	Fifth-order Intermodulation Distortion
IMD:	Intermodulation Distortion
IV:	Current-Voltage
IP_3:	Third-order Intercept Point
IIP_3:	Input Third-order Intercept Point
OIP_3:	Output Third-order Intercept Point
MM:	Metal-to-Metal
MIM:	Metal-Insulator-Metal
PCB:	Printed Circuit Board
PIM:	Passive Intermodulation
P1dB:	1-dB Compression Point

QV:	Charge-Voltage
RL:	Return Loss
RF:	Radio-Frequency
S-parameters:	Scattering parameters
S1P:	1-port S-parameter
TRL:	Through-Reflect-Line
UC:	Unit Cell
VNA:	Vector Network Analyzer
Y2P:	2-port Equation-based Admittance

Contents

CHAPTER 1

Introduction

Over the past few decades, the growth of wireless communication has been tremendous, and this trend is projected to continue. According to Ericssons mobility report from 2022 [1], the number of smartphone subscriptions is forecast to be 6.6 billion by the end of 2022, where the global monthly average usage per smartphone is 19 gigabytes (GB) in 2023. By 2028, the number of smartphone subscriptions is expected to be 7.8 billion, with a monthly average usage per smartphone of 46 GB. To facilitate this growing demand, the capacity of wireless communication needs to be increased, which leads to higher frequency, bandwidth, input power, number of input/output signals, and more communication systems that have to co-exist. These factors increase the risk of interference between communication systems, which degrade the system's performance or, in the worst case, block the radio communication.

There are several types of interference that can range from noise to adjacent channel interference from an external system. In this thesis, interference from unwanted spurious signals is considered, which is known as intermodulation (IM) distortion (IMD) products. The intermodulation products emerge when two or more input signals are present in a nonlinear system. The input signals are mixed, and a wide range of frequency components are generated, covering the in-band, fundamentals, and harmonics. Many of these spurious signals, like the harmonic products, are removed by filters. However, the third-order intermodulation (IM_3) products are in close proximity to the fundamental tones, which makes a filter not suitable as it would also affect the fundamental

tones. The IMD can be generated both internally in a system, but there are also external sources in the form of any metal object, e.g., antennas, tower infrastructure, and metal fences. When these metal objects are radiated, they can generate intermodulation that may be radiated back to a communication system.

The probability of interference from intermodulation increases when the frequency spectrum becomes more densely populated and signal power increases. When the frequency spectrum becomes increasingly crowded, with more co-existing communication systems with similar frequency-bands, the risk increases that one system generate intermodulation products within the same frequency-band as another system's receiver. This issue is more prominent for wideband modulated signals, as the intermodulation product's bandwidth is proportional to the order, e.g., a fifth-order intermodulation (IM_5) product has a bandwidth five times as large as the carrier bandwidth. With an increase in input power, the amplitude of the intermodulation products increases with the order. An increase of 1 dB input power will result in an increased power of 3 dB and 5 dB for the third- and fifth-order intermodulation products, respectively. A nonlinear device can be considered linear for certain power conditions, however the addition of higher power may put them into a nonlinear regime. Therefore, this will increase the requirements on highly linear devices. To be able to meet these requirements, accurate models of nonlinear behavior are imperative to understand and mitigate distortion.

Active circuits can exhibit highly nonlinear behavior, meaning their input and output are not linearly related. Therefore, they are typically operated within an operating condition where it has a more linear behaviour. The current–voltage (IV) and charge-voltage (QV) characteristics often describe the nonlinearity. Examples of nonlinear circuits include amplifiers, mixers, and multipliers, which frequently rely on nonlinear components like transistors and diodes. Various models have been developed to describe the behavior of these circuits, e.g., empirical models that use an equivalent circuit [2] and behavioral modeling [3]. While these models have advanced significantly, development is still ongoing.

Intermodulation distortion is differentiated for active and passive devices by referring to passive intermodulation (PIM) if it occurs in a passive device. However, the phenomenon is the same in both cases, i.e., two or more signals interact with a nonlinear element. The development of modeling the nonlinear behavior in passive components has not received the same attention as active devices. This is because passive structures can typically be represented by linear models over a wide range of power levels. The nonlinear sources in passive components are weakly nonlinear, and high power levels are required

to generate detectable PIM. The difficulty of modeling passive structures is also a factor in the underdevelopment of nonlinear models. Determining which source is responsible for generating PIM can be challenging because multiple sources co-exist in the same system. Nevertheless, several physical sources of PIM have been proposed, including constriction resistance [4], electro-thermal induced PIM [5], tunneling [6], and nonlinear conductivity [7]. These types of sources have been studied in several components, e.g., waveguides [6], [8], coaxial connectors [9], transmission lines [10], [11], and antennas [12]. PIM is a critical issue in satellite communication systems, primarily due to high transmitting power and the susceptibility of receivers. In some cases, the PIM requirements can be as low as -140 dBm [13], making it a major concern for the satellite industry. Consequently, a significant amount of research on PIM is focused on addressing the specific needs of satellite communication systems.

The objective of this thesis is to analyze and model the intermodulation effects that occur in a periodic structure, specifically in a loaded-line phase shifter that uses shunt-loaded varactor-diodes. The nonlinear behavior of the varactor-diodes introduces intermodulation distortion that can negatively impact the overall system performance, such as producing a degraded lobe pattern in active electronically steerable arrays (AESA). The purpose of this is twofold: Firstly, to investigate how the periodically nonlinear loading of the varactor-diodes affects intermodulation generation and to enhance the phase shifter's performance in terms of linearity and phase-shift/loss. Secondly, to provide a deeper understanding of distributed PIM and utilization for future work. In [10], [14], PIM has been studied in transmission lines where the nonlinear sources are predicted to be distributed over the transmission line. The nonlinear sources can be viewed as point sources that generate PIM in the forward and backward direction. PIM from each source can either be added cumulatively from constructive interference or reduced from destructive interference. This depends on the distance between sources and the direction of PIM. In the loaded-line phase shifter, the location and the nonlinear sources are known, which simplifies the analysis and may provide an understanding of the problem.

This thesis has the following structure. Chapter 2 presents the fundamentals of nonlinear distortion. The chapter describes how nonlinear devices generate new frequency content, emphasizing intermodulation distortion. Moreover, some sources of passive intermodulation are described. Additionally, a general overview of some common methods for the analysis of nonlinear devices are presented. Chapter 3 provides a background and utilization of periodic structures and presents the design of a loaded-line phase shifter implemented as a periodic structure. Chapter 4 begins with describing the modeling process and

parameter extraction of a varactor-diode based on Paper C. Then, it presents the realized loaded-line phase shifters from Paper A, Paper B, and Paper C. The results in terms of phase shifter performance and linearity are then presented and compared. Chapter 5 reports on an investigation of whether there is an optimum design of loaded-line phase shifters with respect to both phase-shift/loss and linearity, which is based on Paper C. Finally, Chapter 6 concludes this work and discusses future work.

CHAPTER 2

Fundamentals of nonlinear distortion

This chapter presents fundamental theory of nonlinear distortion. Section. 2.1 gives a mathematical description of how nonlinear devices generate new frequency content with an emphasis on intermodulation distortion. Section. 2.3 describes nonlinear distortion in passive devices. Finally, Section. 2.3 presents methods for analyzing nonlinear devices.

2.1 Intermodulation distortion

To describe the generation of IMD products, a nonlinear system with a sinusoidal input signal with frequency f_1 will first be considered. The input signal can be described as $x(t) = A\cos(\omega t)$, where A is the amplitude of the signal, and the output can be obtained with the Taylor expansion

$$y(t) = a_1 x(t) + a_2 x^2(t) + a_3 x^3(t) ... + a_n x^n(t), \tag{2.1}$$

where a_n is the nth-order Taylor coefficient, which is determined around a bias point X_0 and is calculated by

$$a_n = \frac{1}{n!} \frac{d^n y(X_0)}{dx^n}. \tag{2.2}$$

The result of the output signal with the sinusodial signal is

$$y(t) = \frac{1}{2}a_2A^2 + \left(a_1A + \frac{3}{4}a_3A^3\right)\cos(\omega t) + \frac{1}{2}a_2A^2\cos(2\omega t) + \frac{1}{4}a_3A^3\cos(3\omega t) + ... \tag{2.3}$$

The result of (2.3) shows that the single input excitation has generated several signals. Two factors are related to the fundamental frequency, where the factor a_1A is the gain of the signal and $\frac{3}{4}a_3A^3$ represents the compression. The term $\frac{1}{2}a_2A^2$ represents a DC shift. The other two components are the second harmonic and third harmonic that have the amplitude of $\frac{1}{2}a_2A^2$ and $\frac{1}{4}a_3A^3$, respectively.

If the input instead contains two sinusoidal signals with the same amplitude A and frequency components of ω_1 and ω_2, $x(t) = A\cos(\omega_1 t) + A\cos(\omega_2 t)$, then the result of the Taylor expansion is

$$y(t) = a_2A^2 + \left(a_1A + \frac{9}{4}a_3A^3\right)\cos(\omega_{1,2}t) + \frac{1}{2}a_2A^2\cos(2\omega_{1,2}t) + \frac{1}{4}a_3A^3\cos(3\omega_{1,2}t) + a_2A^2\cos(\omega_1 \pm \omega_2) + \frac{3}{4}a_3A^3\cos(2\omega_{1,2} \pm \omega_{2,1}). \tag{2.4}$$

The Taylor expansion with the two-tone excitation also generates a DC shift and harmonics, but also a set of new signals that is a mix of the frequency components ω_1 and ω_2. These new signals are the intermodulation products. The term $a_2A^2\cos(\omega_1 \pm \omega_2)$ is the second order intermodulation (IM_2) product, and the term $\frac{3}{4}a_3A^3\cos(2\omega_{1,2} \pm \omega_{2,1})$ is the third order intermodulation product. The frequency of the intermodulation products can be calculated as $f_{IM} = |mf_1 \pm nf_2|$, where f_1 and f_2 are the two fundamental frequencies, and m and n are integers that gives the intermodulation order $N = m + n$. The two-tone frequency spectrum of order 3 is presented in Fig. 2.1. It is clear from the figure, that the frequency components at the baseband and the harmonics can be removed by filters. The frequency content in close proximity to the fundamental tones of f_1 and f_2 cannot be filtered out as it will affect the fundamental tones as well. The IM_3 product is closest to the fundamental tones and it is the IMD product that is often causing the greatest problems. The amplitude of the IMD products is reducing with increasing order, and the IM_3 has the largest amplitude of the uneven IMD products. Due to its amplitude and its close proximity to the fundamental tones, the IM_3 is generally of main

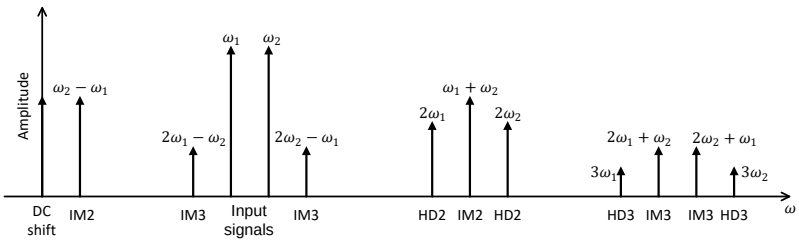

Figure 2.1. The two-tone frequency spectrum illustrated to the third-order, where the two fundamental tones has the frequency of f_1 and f_2.

interest when studying a nonlinear system.

The relationship between output and input power is of interest when studying a nonlinear system. Fig. 2.2 depicts the output power as a function of input power for one of the fundamental signals and one of the IM_3 products. At small input power, the fundamental output power increases with 1 dB when the input power is increased with 1 dB, resulting in a slope of 1 dB/dB. The slope for a higher order signal is proportional to the order of the signal. Therefore, a IM_3 product has a slope of 3 dB/dB and a IM_5 product has a slope of 5 dB/dB. This linear relationship stops at large input signals due to compression. A metric utilized to know when a device goes into compression is the 1-dB compression point (P1dB), which is defined as when the output power decreased 1 dB compared to an extrapolated line of its linear relationship at small input power. To characterize a device's linearity, the linear relationship is extrapolated for both the fundamental tone and the IM_3 product, and the intersection of these two lines is called the third-order intercept point (IP_3). The intercept point will correspond to an input power (IIP_3) and output power (OIP_3), and a greater value of IIP_3 or OIP_3 indicate a more linear device. Intercept points of higher-order are sometimes employed to characterize the linearity, however, the IP_3 is most commonly utilized.

2.2 Passive intermodulation distortion

Intermodulation distortion is commonly associated with active components that are known to be nonlinear. When intermodulation is generated in a passive component it is called passive intermodulation (PIM), however, it is the same phenomenon where two or more signals pass through a nonlinear element that produces mixing products of the input signals. Most passive elements are assumed to be linear. However, all passive components have intrinsic weakly nonlinear sources that can generate PIM with large enough input power. PIM

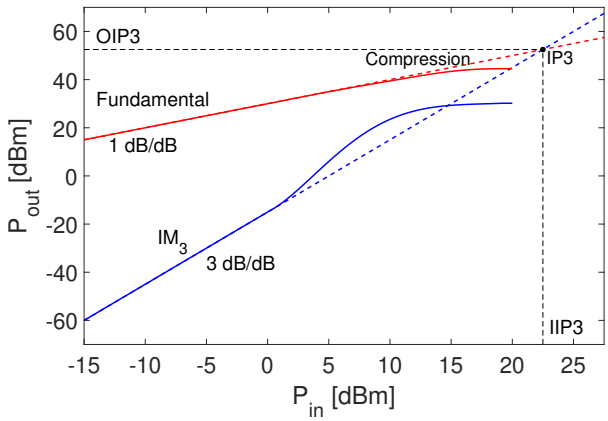

Figure 2.2. The relationship between output and input power of the fundamental tone and the third-order intermodulation. The dashed lines show the extrapolations of the fundamental tone and the third-order intermodulation and their intersection is the third-order intercept point.

is also an issue in systems with high demands on the dynamic range. In satellite communication systems, PIM is a major problem due to high power levels and sensitive receivers, with PIM requirements of -140 dBm [13]. Satellites are often composed of various communication systems that both have transmitters and receivers, which create high demands for these to not interfere with each other. The increased demand of high data rates in satellite communication systems and telecommunications, is increasing the input power and the number of signal carriers, which in turn makes PIM a growing concern. Modeling PIM is a complex problem because several potential PIM sources can exist in a system. It is common to use different "rules of thumb" to avoid PIM, such as avoiding ferromagnetic materials, avoiding dissimilar metal contacts, applying enough contact pressure to metal-to-metal contact, etc. However, a number of physical sources have been described to generate PIM. A few examples are, ferroelectrical and piezoelectrical materials, metal-to-metal (MM) and metal-insulator-metal (MIM) contacts, tunneling, nonlinear conductivity, and constriction resistances. A more in depth explanation of some sources are presented in the following section.

2.2.1 Sources of passive intermodulation

Metallic contacts

The connection between two metals can generate PIM, which have been studied for several components, e.g., coaxial connectors [9], [15]–[17], waveguide flanges [6], [8], [18], [19], and wire mesh antennas [12], [20]–[22]. The contact area between two metals is only a small fraction of the total area due to the surface roughness, as depicted in Fig. 2.3. This creates void regions and contact regions. Metals have a natural insulation layer of oxidation or sulphides, and the thickness of the insulation layer depends on the type of metal, e.g., gold has a thin or no insulation layer, whereas aluminum typically has an oxidation layer of 3 nm thickness. Therefore, the contact points between two metals have two types, MIM contact or MM contact. If an insulating layer exists, the MM contact is formed by applying enough contact pressure to break the insulating layer. In [6], the generation of PIM in the metallic contact between waveguide flanges was studied. They employed the surface model from [23] and the result from [24] to model the connection between two metals. The surface model utilizes a statistical approach that distributes asperities (peaks on the surface) over the surface. Fig. 2.4 depicts the topography of the surface model where one surface is modeled as flat, and the other is modeled as a rough surface with spherical asperities. The asperities are assumed to have the same radius of curvature r, z is the asperity height and is assumed to have a Gaussian distribution, d is the distance between the mean of asperity heights and the flat surface, and l is the interference distance (the distance of the asperity that penetrates the flat surface).

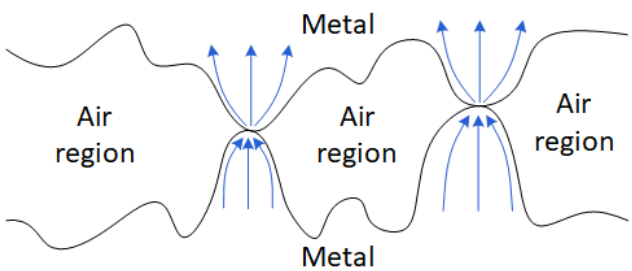

Figure 2.3. Illustration of the rough surface contact between two metals. The blue lines represents the constriction current due to the limited contact area.

Several nonlinear phenomenons that generate PIM in metallic contacts have been proposed, and the type of nonlinearity depends if there is a void region, a MIM contact, or a MM contact. In the void region, the nonlinearity is

associated with field emission or gas breakdown (corona) [6]. MIM contact zones can generate PIM from tunneling, thermionic emission, or the Poole-Frenkel effect. In the MM contact zones, the PIM is generated by constriction resistance, which is related to the change in the direction of the current lines in the area between the MM contact.

The insulating layer in a MIM contact function as a potential barrier, where a current can flow through due to the tunneling effect. For a wave to propagate through the insulating layer depends on the amplitude of the wave function and the energy of the barrier, i.e., the width of the barrier. The wave will decay exponentially through the barrier and if the amplitude of the wave is large enough, some of its energy will decay to the other side. A model for the tunneling effect in MIM contacts is described in [25], which gives an I-V relation for the tunneling current. The model has been employed in [26] and [6] to demonstrate the generation of PIM in MIM contacts.

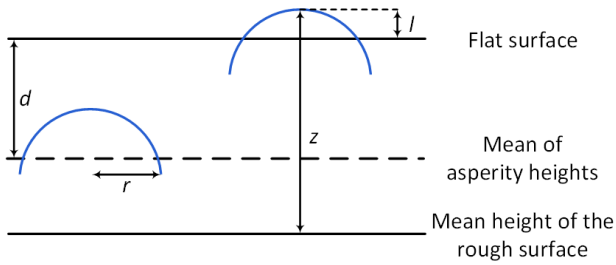

Figure 2.4. The topography of the surface model employed in [6].

Electro-thermal effects

PIM can be generated in lossy passive components through coupling between the electrical and thermal domain. The electro-thermal distortion was studied for lossy passive components in [5], [27]. The electrical and thermal domains have time constants that differentiate by several order of magnitude. However, an interaction between the two domains is possible if the modulated radio-frequency (RF) signal has baseband components that has a period comparable to the thermal time constant. This creates a strong coupling between the electrical and thermal domain and result in an electro-thermal distortion. The coupling is induced from self-heating in resistive materials when high power RF signals are applied. If two or more RF signals are applied, a time varying signal envelope will exist. If the power envelope contains the baseband frequency components, the resistance will vary from periodic heating and cooling. This will effectively function as a passive mixer that will upconvert the envelope

frequencies, and result in PIM.

To understand the coupling between the electrical and thermal domain, we begin with the resistance of a metal. The metal has an electrical resistance and a thermally-based resistance [28]. From the thermally-based resistance, a specific resistance ρ_e can be modeled that also includes the temperature dependence

$$\rho_e(T) = \rho_{e0}(1 + \alpha T + \beta T^2 + ...), \tag{2.5}$$

where T is the temperature, ρ_{e0} is the static resistivity and α and β are temperature coefficients of resistance. The coupling of the thermal and electrical domain is generated from dissipated electrical power, which depends on the current density and the specific resistance of the material. The dissipated electrical power is called self-heating and is expressed as

$$Q = J^2 \rho_e, \tag{2.6}$$

where J is the current density. The heat generated by self-heating is then transferred in the material, which can be described with the heat conduction equation

$$\nabla \cdot \left(\frac{\nabla T}{R_{th}} \right) - C_v \frac{\partial T}{\partial t} = Q, \tag{2.7}$$

where R_{th} is the thermal resistance and C_v is the thermal capacity at constant volume. The thermal resistance is the ability of a material to resist the flow of heat through it. The thermal capacity represents the material's capacity to store heat and its ability to conduct heat to its surroundings. The nonlinear system describing the electrical and thermal coupling is found by substituting 2.5 and 2.6 into 2.7, and is described as follows

$$\nabla \cdot \left(\frac{\nabla T}{R_{th}} \right) - C_v \frac{\partial T}{\partial t} = J^2 \rho_{e0}(1 + \alpha T + \beta T^2 + ...). \tag{2.8}$$

The nonlinear electro-thermal process has a static and a dynamic part with the respective power signals P_s and P_d, dissipating through the static and dynamic resistance R_s and R_d, respectively. The total power dissipated over the static and dynamic resistance is converted to the heat signal $Q\,(P_s + P_d)$. The thermal resistance and capacitance constitute a low pass filter, and the heat signal will be filtered by this thermal response. Fig. 2.5a shows the spectrum of a two-tone signal that is applied to a restive element. The two-tone signal will have a time-varying signal envelope. The instantaneous power of the signal envelope will vary periodically at the beat frequency of the two-tone signal,

and Fig. 2.5b depicts the sum and difference frequency components. This will, in turn, create periodic cooling and heating at baseband frequencies as long as the beat frequency is within the bandwidth of the lowpass filter, as depicted in Fig. 2.5c. The resistance will also vary periodically. This periodic oscillation will result in a passive mixer generating IMD by up-converting the envelope frequencies to RF frequencies, as shown in Fig. 2.5d.

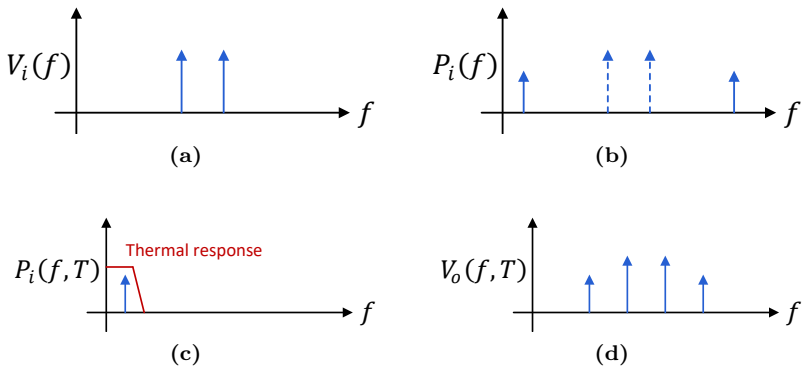

Figure 2.5. Electro-thermal distortion generated in a resistive element by a two-tone excitation. (a) The spectrum of the input voltages. (b) The input power spectrum resulting from the two-tone spectrum. (c) The baseband component of the input spectrum that is within the thermal response. (d) The resulting output spectrum generated from electro-thermal mixing.

2.3 Methods for analysis of nonlinear devices

There exist several methods to analyze nonlinear components or circuits. The three main nonlinear analysis methods are time-domain techniques, harmonic balance and Volterra series. The methods have different advantages and drawbacks, and their suitability depends on the type of circuit and amplitude of the input signal. A general overview of the three methods is presented in this section.

2.3.1 Time-domain techniques

Time-domain techniques are often employed in circuit simulators to solve distortion problems numerically. Time-domain methods solve nonlinear differential equations where incremental time-steps approximate the time derivatives. The time-step selection is often dynamic and depends on the solution's rate

of change, as it decreases the simulation time. This type of solution, called time-step integration, solves the differential equation as an initial value problem [29]. Therefore, the first step is to solve the equation at the starting time t_0, and then each time-step is solved successively. This makes time-step integration suitable for solving transient responses, however, it is not optimal for solving steady-state problems as the transient response has to be solved first. Other issues arising when determining distortion with time-step integration is first that the circuit has to be in a periodic steady state before performing a Fourier analysis to obtain the frequency response. Fast Fourier transform (FFT) requires a uniform grid of samples that has to be interpolated in the case of dynamically selected time-steps, which can result in errors [30]. In circuits with vastly different time constants, the number of time-steps has to be large, which results in long simulation times. In the case of solving circuits with small distortion amplitudes, the number of time-steps also has to be significant because, otherwise, the small distortion components will be masked by the numerical noise floor. The shooting-Newton and finite-difference in time-domain (FDTD) methods circumvent the cumbersome calculation of the transient response. However, all time-domain methods have a common problem with circuit element that has a frequency-domain representation, e.g., dispersive transmission lines and measured scattering matrix. Instead, frequency-domain solvers can be utilized such as harmonic balance and Volterra series. The main advantage of solving distortion problems in the time-domain is handling of strong nonlinear problems.

2.3.2 Harmonic balance

The harmonic balance method is a standard tool to simulate nonlinear distortion problems numerically. The harmonic balance is a frequency-domain solver that manages two or more signals with independent frequencies with vastly different amplitudes and time scales, in contrast to the time-domain techniques. Additionally, it handles components with a frequency-domain representation. The steady-state response is solved directly in the harmonic balance method by assuming that the steady-state response is composed of sinusoids, and the coefficients of the sinusoids that satisfies the differential equation are obtained by the method [31].

The following text describes the conceptual idea of the harmonic balance method, where a circuit is rearranged into a linear subcircuit and a nonlinear subcircuit [32], as shown in Fig. 2.6. The linear part is solved in the frequency-domain, and the subcircuit is described by a multiport matrix, e.g., its Y-parameters or S-parameters. A $N \times (N + M)$ matrix describes the linear subcircuit, where N is the number of common ports of the two subcircuits, and

M is the number of additional external sources. The linear circuit also includes the source and load impedances and parasitics of the nonlinear elements.

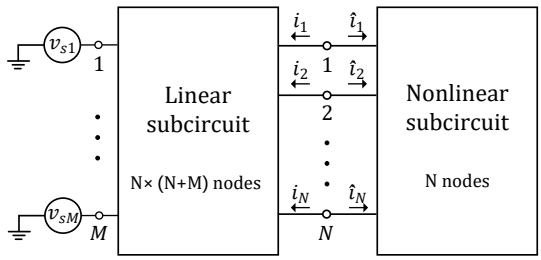

Figure 2.6. The circuit in the harmonic balance method rearranged into a linear subcircuit and a nonlinear subcircuit that shares N common nodes. The external sources are fed to the linear circuit and share M number of nodes.

The nonlinear subcircuit is solved in the time-domain because models of the nonlinear components in the frequency-domain are not possible [33]. In the common nodes connecting the two subcircuits, there are two currents, one that is linear $\mathbf{I}$ and one that is nonlinear $\hat{\mathbf{I}}$. The linear current can be solved by multiplying the admittance matrix with the voltages, which contain all common nodes and external sources. The expression of nonlinear current depends on the nonlinear components, i.e., nonlinear capacitors or conductors. The nonlinear current is evaluated in the time-domain, which is then converted to frequency-domain by Fourier transform. The goal of the harmonic balance is to find a set of port voltages waveforms that generate equal linear and nonlinear currents, which can be described as

$$\mathbf{F}(\mathbf{V}) = \mathbf{I} + \hat{\mathbf{I}} = \mathbf{0}, \tag{2.9}$$

where $\mathbf{F}(\mathbf{V})$ is the current-error vector, $\mathbf{V}$ is the set of node voltages waveforms, and $\mathbf{0}$ is the zero vector. The correct solution is obtained when $\mathbf{V}$ generates $\mathbf{F}(\mathbf{V}) = \mathbf{0}$. The currents in (2.9) are solved for all common ports N and the number of selected harmonics K. Therefore, the linear current $\mathbf{I}$ is described by

$$\mathbf{I} = \begin{bmatrix} I_{1,0} \\ I_{1,1} \\ \cdot \\ \cdot \\ \cdot \\ I_{1,K} \\ I_{2,0} \\ \cdot \\ \cdot \\ \cdot \\ I_{2,K} \\ \cdot \\ \cdot \\ \cdot \\ I_{N,K} \end{bmatrix}. \tag{2.10}$$

The nonlinear current is described equivalently. To summarize the process, first, a set of $\mathbf{V}$ is initially guessed and the linear and nonlinear currents are solved. To solve the nonlinear current, $\mathbf{V}$ has to be converted to time-domain, then the nonlinear current is solved in time-domain, which is then converted to frequency-domain. Then the current error-vector $\mathbf{F}(\mathbf{V})$ is then evaluated. The process stops if $\mathbf{V}$ satisfies the solution, otherwise, another set of $\mathbf{V}$ is tried until a solution is found.

Some difficulties for the harmonic balance are strongly nonlinear circuits or if there are signals with abrupt transitions [33], i.e., square waves and narrow pulses. The harmonic balance may suffer of convergence problems when the circuit is strongly nonlinear. To represent signals with abrupt transitions many frequencies are needed, which increases the computational complexity. Furthermore, for a signal with a sharp transition, the magnitude of the harmonic drops slowly, which increases the number of harmonics needed to obtain accurate results, and this also increases the computational complexity.

2.3.3 Volterra analysis

The Volterra series is an analytical method where the nonlinearities can be described with closed form expression. Therefore, it gives insight to the nonlinear behavior and is suitable both for analyzing and designing circuits. The Volterra series describes the output of a nonlinear system as a combination of operators of different orders [34], which is represented in Fig. 2.7. The operators $\mathbf{H_1}$, $\mathbf{H_2}$, $\mathbf{H_3}$, $\mathbf{H_n}$ are of the first-, second-, third-, and nth-order. If

the third-order operator is considered in time-domain with an input signal $x(t)$ then it can be mathematically described by

$$\begin{aligned} \boldsymbol{H}_3[x(t)] = \int_{-\infty}^{+\infty} \int_{-\infty}^{+\infty} \int_{-\infty}^{+\infty} h_3(\tau_1, \tau_2, \tau_3) \\ x(t-\tau_1)x(t-\tau_2)x(t-\tau_3)d\tau_1 d\tau_2 d\tau_3. \end{aligned} \tag{2.11}$$

The integral is a three-dimensional convolution integral where the third-order nonlinearity is calculated by a third-order convolution of the function $h_3(\tau_1, \tau_2, \tau_3)$ with the input signal. The function function $h_3(\tau_1, \tau_2, \tau_3)$ is a three-dimensional impulse response and is called the third-order Volterra kernel. The Volterra operator can be generalized for the nth-order as

$$\begin{aligned} \boldsymbol{H}_n[x(t)] = \int_{-\infty}^{+\infty} \dots \int_{-\infty}^{+\infty} h_n(\tau_1, \tau_2, \dots, \tau_n) \\ x(t-\tau_1)x(t-\tau_2)\dots x(t-\tau_n)d\tau_1 d\tau_2 \dots d\tau_n. \end{aligned} \tag{2.12}$$

The final expression to calculate the output of the system is represented in Fig. 2.7, which becomes

$$y(t) = \boldsymbol{H}_1[x(t)] + \boldsymbol{H}_2[x(t)] + \dots + \boldsymbol{H}_n[x(t)]. \tag{2.13}$$

Here the Volterra series is represented in the time-domain. However, it is also possible to represent in the frequency-domain, and is commonly employed in the frequency-domain as it simplify the analysis of circuit elements with frequency-domain representation. The Volterra series handles elements with memory effects which makes it suitable for circuits with inductors, capacitances, and/or feedback. If the circuit does not have memory effects, the Volterra series reduces to a power series.

The Volterra series has many advantages, such as not relying on iterative methods, giving insight into the nonlinear behavior by closed-form expressions, handling components with frequency-domain representation, and having no restrictions on the excitation signal spectrum. However, a significant drawback is that it cannot handle large nonlinear problems. The Volterra series has a convergence problem and is often limited to an order of five [29]. Therefore, the analysis is restricted to weakly nonlinear circuits.

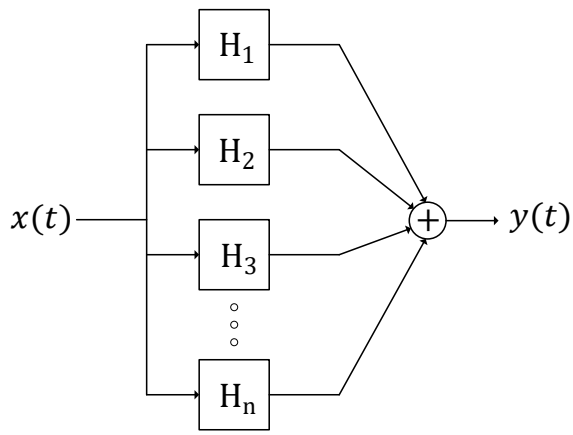

Figure 2.7. A schematic illustrating how the Volterra kernels act on the input signal $x(t)$ to generate the nonlinear output $y(t)$.

CHAPTER 3

Periodic structures

This chapter gives a background and the utilization of periodic structures. Section 3.1 presents the main characteristics of periodic structures and how these characteristics are achieved. Section 3.2 presents the design of loaded-line phase shifters implemented as a periodic structure. Additionally, the performance metrics of a phase shifter are described.

3.1 Basics of periodic structures

Periodic structures are composed of a medium of electromagnetic waves, e.g., transmission lines and waveguides, that are periodically loaded by reactive elements. The reactive elements can be either a discontinuity in the medium or a lumped component in a transmission line. Periodic structures have two special characteristics, which are passband-stopband response and the ability to support waves with phase velocities less than the speed of light [35]. These characteristics are employed to modify electromagnetic waves, e.g., traveling-wave tubes [36], filters [35], phase shifters [37], and steerable antennas [38]. To illustrate how these characteristics are obtained, a periodically loaded transmission line is considered in Fig. 3.1. The figure illustrates two cases, one with shunt capacitive loading and one with series inductive loading.

In a smooth transmission line, it is not possible to change the phase velocity by modifying the geometry. The phase velocity in a transmission line is

$$v_p = \frac{1}{\sqrt{L_t C_t}}, \tag{3.1}$$

where L_t is the series inductance per unit cell length and C_t is the shunt capacitance per unit cell length. Suppose the geometry of the smooth transmission line is changed to increase the shunt capacitance per unit cell length. In that case, it will result in a decreased series inductance per unit cell length, and the phase velocity will stay consistent. The addition of periodic reactive elements enables a change in the phase velocity by increasing the propagation constant β. An unloaded transmission line with low impedance is employed for the transmission line with series inductance in Fig. 3.1a. The loading inductance increases the transmission line's characteristic impedance to its desired value. The opposite happens for the transmission line with shunt capacitive loading in Fig. 3.1b. An unloaded high-impedance transmission line is employed, and the shunt capacitance decreases the characteristic impedance. For a structure with both inductive and capacitive loading [28], the propagation constant is described by

$$\beta = \omega \sqrt{\left(L_t + \frac{L_0}{d}\right)\left(C_t + \frac{C_0}{d}\right)}, \tag{3.2}$$

where L_0/d and C_0/d are the amount of added inductance and capacitance per unit cell length, where L_0 and C_0 are the loading factor of the inductors and capacitors added to the structure with period d.

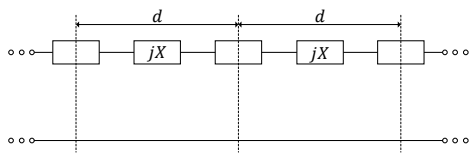

(a)

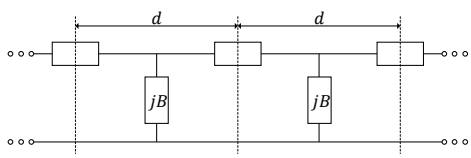

(b)

Figure 3.1. Illustration of a periodically loaded transmission line with (a) series inductance loading, and (b) shunt capacitive loading.

The periodic structure is dispersive and has passbands and stopbands related to the propagation constant of the unloaded medium k_0 and the periodically loaded structure β. This relationship is examined in a $k-\beta$ diagram (Brillouin diagram), where β is plotted as a function of k_0. The Brillouin diagram gives insight into what frequencies that correspond to passbands and stopbands for different modes propagating in the periodic structure. If we consider the periodic structure with capacitive loading in Fig 3.1b, the relation between β and k_0 can be described with the dispersion equation

$$\cos(\beta d) = \cos(k_0 d) - \frac{\bar{B}}{2}\sin(k_0 d), \tag{3.3}$$

where d is the period of the structure, and $\bar{B}$ is the normalized susceptance of the loads. Dispersion is increased with increasing frequency. At low frequencies, the periodic structure has an increased propagation constant that reduces the propagation velocity, which means it supports slow-traveling waves without dispersion. With an increased frequency, the structure's dispersion becomes larger, decreasing the group velocity, and at a high enough frequency, the propagation stops. The condition for the stopbands is that the right-hand side of (3.3) is larger than unity. The lower and upper-frequency limits of the stopbands can be expressed as

$$n\frac{c_0}{2d\sqrt{\epsilon_e}} < f < n\frac{c_0}{2d\sqrt{\epsilon_r}}, \tag{3.4}$$

where ϵ_e is the effective permittivity of the periodic structure, ϵ_0 is the permittivity of the unloaded transmission line, n is the order of the stopband, and c_0 is the speed of light in free space. The upper limit is called the Bragg frequency f_B, which occurs when d is equal to half of the wavelength of the unloaded transmission line and is, therefore, not dependent on the periodic loading. However, the lower limit depends on $\bar{B}$ and occurs when d is equal to half of the wavelength of the periodic structure.

3.2 Design of a loaded-line phase shifter

A tunable phase shifter has the purpose of modifying the phase shift or the group delay of a transmitted signal with the smallest possible loss. There are several implementations of tunable phase shifters, e.g., switched-line phase shifters, hybrid-coupled reflection-type phase shifters [39]–[41] and loaded-line phase-shifters [37], [42]. Only the two latter may be used for analogue tuning, and loaded-line phase shifters have advantages due to ease of implementation and relatively low loss if moderate orders of phase shift are needed [43]. Types

of tuning mechanisms are mechanical, magnetic, and electric. In many modern applications, e.g., AESA, only electronic steering is relevant. In the past, exotic tuning mechanisms such as ferroelectric varactors have been evaluated for low loss with promising results [44], [45]. However, for ease of manufacturing, compatibility with active components technology, and still very competitive performance, semiconductor varactor diodes are still the most commonly used [37]. In the following text, the design basics of a loaded-line phase shifter and the different performance metrics are presented.

A loaded-line phase shifter is composed of a transmission line periodically loaded by shunt-susceptances. Varactor-diodes are commonly employed as the loading, as depicted in Fig 3.2. The varactor-diodes are reversed biased. Therefore, they are modeled as a nonlinear capacitor and share similarities with the design in Fig. 3.1b, where we wanted a high-impedance unloaded transmission line. In the illustration of the loaded-line phase shifter, there is a T-unit cell (UC) that consists of two transmission lines of length $d/2$, and with a shunt-loaded varactor diode in between. The transmission line has an inductance per unit cell length L_t and a capacitance per unit cell length C_t. The varactor-diode has a voltage-controlled capacitance $C_V(V_R)$, where V_R is the reversed bias voltage. $C_V(V_R)$ is the loading capacitance in this design. The transmission line has an unloaded impedance Z_0, and the effective characteristic impedance Z_e of the unit cell can be calculated with

$$Z_e = \sqrt{\frac{L_t}{C_t + C_V/d}}. \tag{3.5}$$

The equation is valid as long as the frequency is far below the Bragg frequency. In terms of the loaded-line phase shifter parameters, the Bragg frequency [46] is

$$f_B = \frac{1}{\pi\sqrt{L_t d(C_t d + C_V)}}. \tag{3.6}$$

Under the condition $C_V \gg C_t$, (3.5) can be simplified to

$$Z_e = \sqrt{\frac{L}{C_V}}, \tag{3.7}$$

where L is the inductance per unit cell, i.e., $L = L_t d$. To achieve a large phase shift, both L and C_V shall be large, and to obtain a large L the unloaded transmission line needs to be of high-impedance. The capacitance $C_V(V_R)$ changes with the bias condition, and only one bias point will achieve a perfect match with the system impedance. Therefore, the phase shifter will be mismatched when tuning the phase and there will be two extreme bias points

of $V_{\min}$ and $V_{\max}$. When designing a phase shifter, the differential phase shift $\Delta\phi$ is of interest, which is defined as the phase shift between the two extreme bias points and is expressed as follows

$$\Delta\phi = \beta(V_{\min}) - \beta(V_{\max}). \tag{3.8}$$

In reality, an increased phase shift normally comes with increased attenuation due to mismatch and dissipation. Therefore, phase shifters are also evaluated for a phase-shift/loss figure of merit (FOM). The FOM is expressed as

$$F_{\Delta\phi} = \frac{\Delta\phi_{\text{degree}}}{L_{\text{dB}}}, \tag{3.9}$$

where L_{dB} is the total loss in the phase shifter. The total loss will vary depending on the applied bias, and in this work, L_{dB} is defined as the total loss for the bias state with the most significant loss.

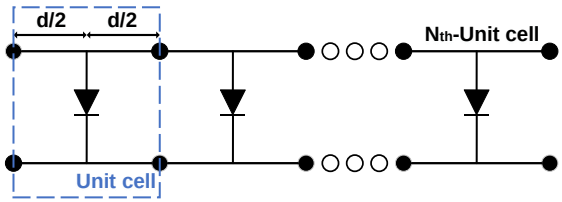

Figure 3.2. Illustration of a periodic loaded-line phase shifter loaded by varactor-diodes.

CHAPTER 4

Intermodulation in loaded-line phase shifter

The previous chapter presented the theory of periodic structures. Starting from this basis of the theory, Section 4.1 provides the design of a loaded-line phase shifter implemented in PCB technology with shunt-loaded varactor-diodes. Section 4.2 describes the varactor-diode model and the extraction of the model parameters. Then, the realized phase shifters are presented in Section 4.3. Finally, the experimental results are presented in Section 4.4.

4.1 Phase shifter design

The loaded-line phase shifters presented in this chapter are implemented in PCB technology with shunt-loaded varactor-diodes. An illustration of a periodic loaded-line phase shifter composed of N number of T-unit cells is depicted in Fig. 4.1. The T-unit cell consists of two transmission lines of length $d/2$, and with a shunt-loaded varactor-diode in between. The varactor-diode has a voltage-controlled capacitance $C_V(V_R)$, where V_R is the reversed bias voltage. The varactor-diode is the tuning element of the phase shifter that modifies the phase by varying V_R. The transmission line has a high unloaded impedance Z_0 and a physical length θ_0. The effective characteristic impedance Z_e and the effective electrical length θ_e are determined by the loading capacitance C_v, Z_0 and θ_0. The size of the loading capacitance affects the phase shift where a large C_v creates a large phase shift.

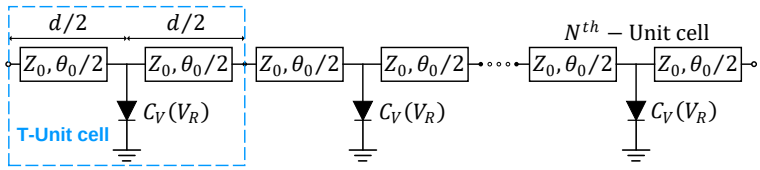

Figure 4.1. Illustration of the periodic loaded-line phase shifter with N number of T-unit cells.

4.2 Varactor-diode modeling

To correctly evaluate the performance of a loaded-line phase shifter in simulation, an accurate varactor model has to be implemented, especially to describe the nonlinear behavior of the phase shifter. Under normal operation the varactor-diodes in a loaded-line phase shifter are reversed biased and, therefore, the nonlinear capacitance of the varactor is of primary interest in the model. An equivalent circuit model of the reversed bias varactor is presented in Fig. 4.2 that is composed of a series inductance (L_s), a series resistance (R_s), a parallel capacitance (C_p), and the variable junction capacitance (C_j). It is common to extract the parameters of the model with the real and imaginary parts of the measured impedance

$$Z(V_R) = R_s + j\left(\omega L_s - \frac{1}{\omega C_V(V_R)}\right), \tag{4.1}$$

where $C_V(V_R) = C_j(V_R) + C_p$. The nonlinear element in the model is the variable junction capacitance. The model of C_j depends on the doping profile of the pn junction. In the case of a uniformly doped and linearly graded junction, the variable junction capacitance is typically modeled as

$$C_j(V_R) = \frac{C_{j0}\phi^n}{(\phi + V_R)^n}, \tag{4.2}$$

where C_{j0} is the zero bias junction capacitance of the diode, ϕ is the built-in potential, and n is the grading coefficient [47]. This model has shown good accuracy for uniform varactor-diodes. However, when the doping profile is highly nonuniform, (4.2) may not accurately describe the C-V characteristics of the varactor-diode. Instead, a piecewise model may be used or a capacitive polynomial series. A capacitive polynomial series can be expressed as

$$C_j(V_R) = C_0 + C_1 V_R + C_2 V_R^2 + ... + C_n V_R^n, \tag{4.3}$$

where C_n is the polynomial coefficient of the n^{th}-order.

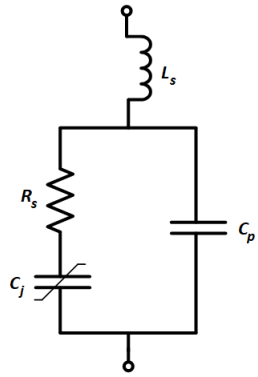

Figure 4.2. Equivalent circuit model of the reversed bias varactor-diode.

4.2.1 Extraction of varactor-diode model parameters

The extraction of the model parameters of the varactor-diode presented here is based on a hyperabrupt varactor of model SMV1233-079LF. However, the process to extract the model parameters could be performed with another varactor-diode as well. The extraction is performed by measuring the S-parameters of the varactor. The varactor was placed in shunt in a two-port network, as depicted in Fig. 4.3a, where the coaxial connectors and transmission lines in the two-port network are de-embedded. The modeled bias range of the varactor should be larger than the bias range of the phase shifter to properly model the nonlinear behavior because it has to cover the RF voltage swing, which includes both DC and RF voltage. Due to the T-network configuration of the measured two-port, the varactor's impedance is equal to Z_{12}. The C-V characteristic is obtained from the imaginary part of (4.1) at a low frequency where the effect of the parasitic inductance is small. A restricting factor can be limited precision in the VNA calibration at low frequency. In the case of the measurement of the hyperabrupt varactor SMV1233-079LF, the C-V characteristic was found at 200 MHz for a bias ranging from 0.3 V to -12 V.

The two models of C_j presented in (4.2) and (4.3) were evaluated for the varactor SMV1233-079LF. The parameters in (4.2) are typically provided by a datasheet. However, some optimization of the parameters may be necessary to obtain an accurate fit of the measured C-V characteristics. In the case of (4.3), the polynomial coefficients are obtained by a polynomial curve fitting of the measured C-V characteristics. In Fig. 4.3b, a comparison of the two

models and the measured C-V characteristics is presented. It shows that the polynomial model (4.3) has an excellent fit over the full bias range, whereas the model in (4.2) has discrepancies. The discrepancies are most likely due to the highly nonuniform varactor-diode, which makes (4.2) inadequate as a model. In the comparison, (4.2) utilizes the datasheet parameters. However, even with optimization of the parameters, it was not possible to have a good agreement between the model and the measured data for the full bias range.

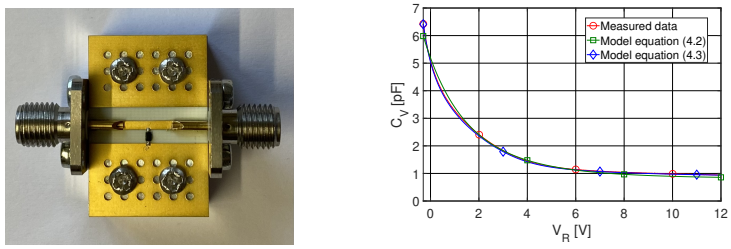

(a) **(b)**

Figure 4.3. The varactor-diode SMV1233-079LF in (a) a two-port network employed for S-parameter measurement, and (b) a comparison of its C-V characteristic between the measured data, the varactor-diode model in (4.2), and the varactor-diode model in (4.3).

The series inductance was obtained from $\mathrm{Im}(Z_{12})$ of the measured varactor impedance. At higher frequencies, L_s has a greater influence on $\mathrm{Im}(Z_{12})$ and to adequately model the nonlinear behavior this influence should be modeled to at least the frequency of the third harmonic. First, L_s was estimated by comparing $\mathrm{Im}(Z_{12})$ at low frequency and at the design frequency. The inductance was then tuned until $\mathrm{Im}(Z_{12}) - \omega L_s$ was constant over frequency for all bias values. The obtained value was 1.51 nH compared to the datasheet value of 0.7 nH. The larger extracted value comes most likely from the soldering and the small pads connecting the varactor. Fig. 4.4a depicts the $\mathrm{Im}(Z_{12})$ for the second and third harmonic, corresponding to 3 GHz and 4.5 GHz, respectively. The second harmonic is inductive at the lower range of V_R, and the third harmonic is inductive over the full range of V_R.

Lastly, the series resistance was found from $\mathrm{Re}(Z_{12})$. The measured resistance versus bias is depicted in Fig. 4.4b. At low frequency, the measurement is noisy, and at higher frequency the resistance increases due to the skin effect and distributed effects in the varactor. The resistance was obtained by finding the average for each frequency and then calculating the average of those averages. The frequencies were limited to 1.5 GHz to 2.5 GHz to avoid the measurement

noise and the skin effect and distributed effects at high frequency. The obtained R_s was 1.49 Ω, which is close to the datasheet value of 1.2 Ω.

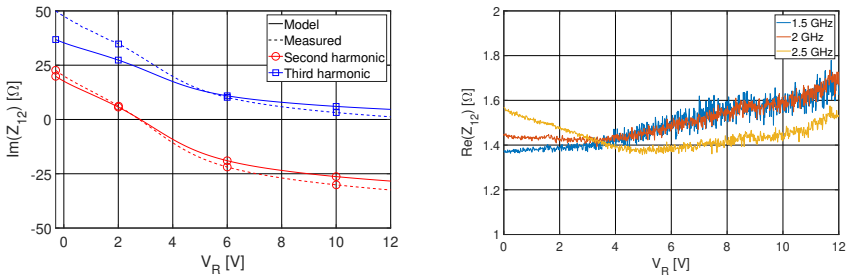

(a) **(b)**

Figure 4.4. (a) Modeled and measured $\mathrm{Im}(Z_{12})$ for the second harmonic (3 GHz) and third harmonic (4.5 GHz). (b) Real part of the measured varactor impedance.

4.3 Realized loaded-line phase shifters

In this section, a number of loaded-line phase shifters are presented. They share similarities such as implementation in a grounded coplanar waveguide (CPWG) configuration with periodically shunt-loaded varactors, the substrate Rogers RO4350 with the relative permittivity $\epsilon_r = 3.66$ and height 0.508 mm, a design frequency of 1.5 GHz, and an effective characteristic impedance $Z_e = 50$ Ω. The main difference is the type of varactor-diode. A BAT63 silicon Schottky varactor-diode is employed in Paper A and Paper B. A hyperabrupt SMV1233-079LF varactor-diode is employed in Paper C.

The loaded-line phase shifters in Paper A and Paper B are the same, but the model was further developed in Paper B. Three phase shifters were fabricated that differ in the number of unit cells, which were 1, 4, and 7 unit cells, as depicted in Fig. 4.5a. The loaded-line phase shifters are designed with a unit cell that has the effective electrical length of 90° at the design frequency with a $Z_0 = 76$ Ω. As shown in Fig. 4.5b, each unit cell is symmetric with two varactor-diodes that are connected to the top and bottom ground plane, and this configuration simplifies appliance of bias as only one bias supply is needed for all varactor-diodes. The varactor-diode is a BAT63 Schottky diode. The C-V characteristic is shown in Fig. 4.5c. At 1 MHz the diode's junction capacitance C_{j0} is 0.75 pF. The reversed bias applied to the phase shifters was varied from 0.3 V to 3 V. The lower and upper limit was selected because at a $V_R < 0.3$ V losses were too high, and at $V_R > 3$ V the tuning saturated.

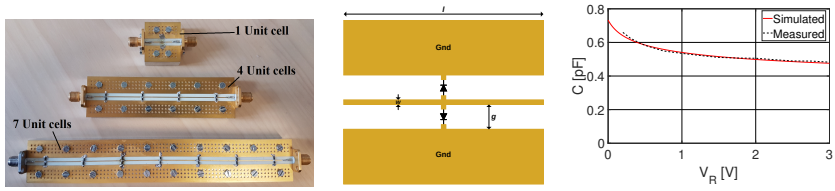

(a) (b) (c)

Figure 4.5. (a) Realized phase shifters with the BAT63 Schottky varactor-diode employed. (b) Illustration of the unit cell design where $w = 0.48$ mm, $l = 22$ mm and $g = 1.9$ mm. (c) Measured and simulated C-V characteristics of the BAT63 Schottky varactor-diode.

Fig. 4.6 depicts six loaded-line phase shifters that were presented in Paper C. The difference between the phase shifters are two different unit cell lengths and the number of unit cells, which are 1, 5, and 10 unit cells. The unit cells were designed to two different θ_e at the center of the tuning range and at the design frequency of 1.5 GHz. The tuning range was selected to be from $V_R = 3$ V to $V_R = 8$ V. The lower limit of V_R was selected because of two reasons. Firstly, there is a risk that the varactor becomes forward bias when V_R is close to zero because of the addition of the RF voltage swing. Secondly, the IL of the phase shifter increases significantly when $V_R < 3$ V, which makes the phase shifter unsuitable in that bias range. The upper limit was selected to avoid the breakdown region, and a larger limit only resulted in minimal gain in terms of tuning range. In Fig. 4.7a, θ_e and Z_e are presented for the two unit cells at the center of the tuning range $V_R = 5.5$ V. The shorter unit cell has a $\theta_e = 57.7°$ at the design frequency and a $Z_0 = 100\ \Omega$. The longer unit cell has a $\theta_e = 66.4°$ at the design frequency and a $Z_0 = 90\ \Omega$. The phase shifters' input and output are connected with a coaxial connector and transmission line denoted as a thru line, which is illustrated in Fig. 4.7b for a single unit cell. To de-embed the effect of the coaxial connector and the transmission line, a Thru-Reflect-Line (TRL) was designed as described in [48], and the TRL design is depicted in Fig. 4.7c. Three lines were fabricated to cover the frequency range from 40 MHz to 4 GHz. A final comment about the design, only one varactor-diode for each unit cell is connected to one of the ground planes compared to Paper A and Paper B which had two varactor-diodes for each unit cell. This is because of the large capacitive value of the SMV1233-079LF varactor. With an increased loading capacitance, the unloaded impedance also has to be increased to maintain a 50 Ω effective characteristic impedance. Therefore, the width of the transmission line became extremely narrow with

two varactor-diodes in a single unit cell, and the design with one varactor-diode was the better option in terms of fabrication.

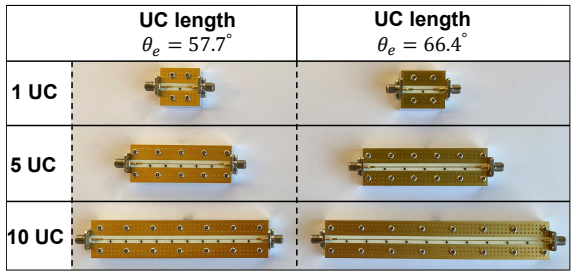

Figure 4.6. The fabricated phase shifters in Paper C.

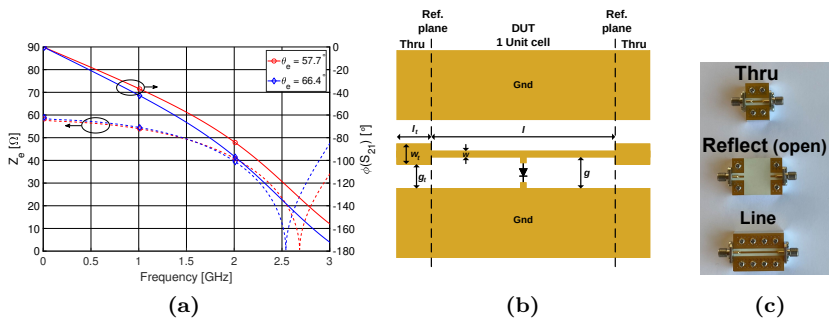

(a) (b) (c)

Figure 4.7. (a) The simulated Z_e and θ_e for the two unit cells. (b) Illustration of the phase shifter with a single unit cell and the thru lines. The dimensions of the unit cell with $\theta_e = 57.7^\circ$ are $l = 10.1$ mm, $w = 0.31$ mm, and $g = 2.34$ mm. The dimensions of the unit cell with $\theta_e = 66.4^\circ$ are $l = 13.14$ mm, $w = 0.4$ mm, and $g = 2.29$ mm. The dimensions of the thru line are $l_t = 8$ mm, $w_t = 1.183$ mm, and $g_t = 1.9$ mm. (c) The fabricated TRL design. The reflect is generated with an open circuit. Three lines were fabricated with line lengths of 18 mm, 83.3 mm, and 386.7 mm.

4.4 Experimental results

This section presents the experimental results of the realized phase shifters from the previous section. The experimental results are split into two parts. The first part contains the phase shifter performance in terms of the differential

phase shift, FOM, insertion loss (IL), phase shift, and return loss (RL). The second part describes the nonlinear behavior of the phase shifters.

4.4.1 Phase shifter performance

The different metrics of performance of the phase shifters were obtained by measuring and simulating the S-parameters. The measurement was carried out with an N5222A PNA Microwave Network Analyzer, and Advanced Design System (ADS) was utilized for the simulations. The results have both the function of evaluating the phase shifter performance and validating the varactor-diode model.

The results presented for the phase shifters with the Schottky varactor-diode are from Paper B, as the model had been further developed. The measured and simulated IL, phase shift and RL are shown in Fig. 4.8. The simulated and measured results have good agreement from DC to the design frequency. At higher frequencies, there are some discrepancies that are probably the result of distributed effects that the model does not capture. Fig. 4.9 depicts the differential phase shift and FOM between $V_{\mathrm{Rmin}} = 0.3$ V and $V_{\mathrm{Rmax}} = 3$ V.

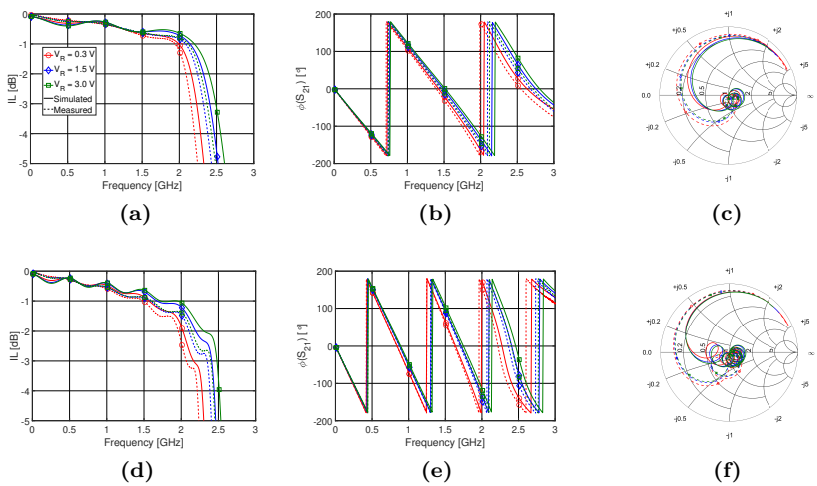

Figure 4.8. The simulated and measured S-parameters for the phase shifter in Paper B. The results for the phase shifter with 4 unit cells (a) IL, (b) phase shift, and (c) $|S_{11}|$. The results for the phase shifter with 7 unit cells (d) IL, (e) phase shift, and (f) $|S_{11}|$.

The IL, phase shift and RL for the phase shifters with a unit cell length of 66.4° in Paper C are presented in Fig. 4.10. The results of the phase

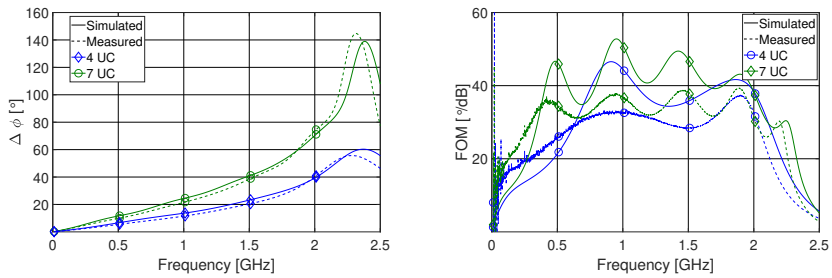

Figure 4.9. (a) The differential phase shift and (b) FOM for the phase shifters with 4 and 7 unit cells in Paper B.

shifters with the shorter unit cell length are similar and omitted for clarity. The simulated and measured result have good agreement. However, there is a deviation for the phase shift after 2 GHz for the phase shifters with 5 and 10 unit cells, and they also have a larger measured IL. Fig. 4.11 depicts the differential phase shift and FOM between $V_{\mathrm{Rmin}} = 3$ V and $V_{\mathrm{Rmax}} = 8$ V. The measured FOM has unrealistic values at low frequency due to limited precision in VNA calibration, which greatly impacts the low insertion loss. The measured FOM is lower than the simulated FOM after 0.5 GHz due to the larger measured IL.

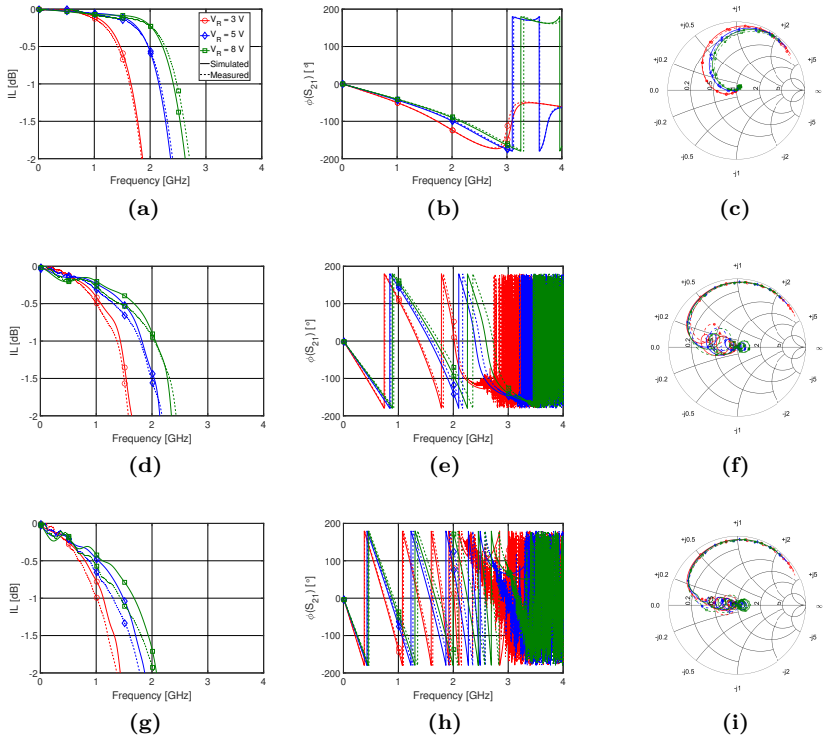

Figure 4.10. The simulated and measured S-parameters for the phase shifter with a unit cell length of 66.4°. The results for the phase shifter with 1 unit cell (a) IL, (b) phase shift, and (c) $|S_{11}|$. The results for the phase shifter with 5 unit cells (d) IL, (e) phase shift, and (f) $|S_{11}|$. The results for the phase shifter with 10 unit cells (g) IL, (h) phase shift, and (i) $|S_{11}|$.

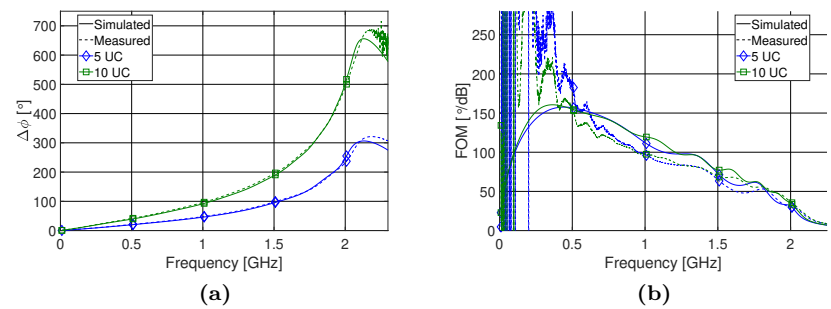

Figure 4.11. (a) The differential phase shift between $V_{\mathrm{Rmin}} = 3$ V and $V_{\mathrm{Rmax}} = 8$ V for and (b) FOM for phase shifters with a unit cell length of 66.4°.

4.4.2 Nonlinear behavior

Nonlinear simulations

The nonlinear behavior of the phase shifter was simulated with harmonic balance algorithm in ADS. The intermodulation products generated in the device under test (DUT) are affected by the impedance connected to the DUT's input and output. Ideally, the measurement system presents 50 Ω to the DUT from baseband to higher-order harmonics for each bias. However, this is rarely the case and will affect the intermodulation generated in the DUT. Therefore, it is imperative to add the impedance connected to the DUT's input and output in the simulation setup. This was first considered in Paper C, where the S-parameters of the measurement setup connected to the input and output of the DUT were measured and added to the simulation setup. The S-parameters of the thru line connected to the DUT, shown in Fig. 4.7b, were also added to the simulation setup. The simulation setup in Paper C is illustrated in Fig. 4.12a. The measured input impedance of the measurement setup was a 1-port S-parameter (S1P) measurement. However, the S1P was converted to a 2-port equation-based admittance (Y2P) component in ADS because of its location between the power source and the thru line in the simulation setup. The power source in ADS has a source impedance of 50 Ω and the equations in Fig. 4.12a show how the correct input impedance is obtained. The two fundamental tones had the frequencies of 1.5 GHz and 1.55 GHz, generating the lower-band and upper-band IM_3 frequencies of 1.45 GHz and 1.6 GHz. The harmonic balance mixing order was set to 5 and all S-parameters were measured up to 15 GHz, which covers well beyond the frequency range of the mixing order. The effect of adding the impedance connected to the DUT's input and output is shown in Fig. 4.12b. The figure shows the measured result compared to different simulation setups. The greatest improvement comes from adding the measured S2P component of the thru. However, the addition of the measurement setup's impedance improves the agreement of simulated and measured IM_3 between 1.5 V and 4 V. In Paper A and Paper B, the influence of the measurement setup was not considered, and the coaxial connectors at the phase shifters input and output was modeled as an LC-network. The values of the LC-network were obtained by optimization versus the measured S parameters. This adds much uncertainty to the model parameters and, therefore, is the simulation method in Paper C preferable.

Nonlinear measurement setup

The IMD in a device is commonly measured with a two-tone test, which is illustrated in Fig. 4.13. The fundamental tones are typically generated by two

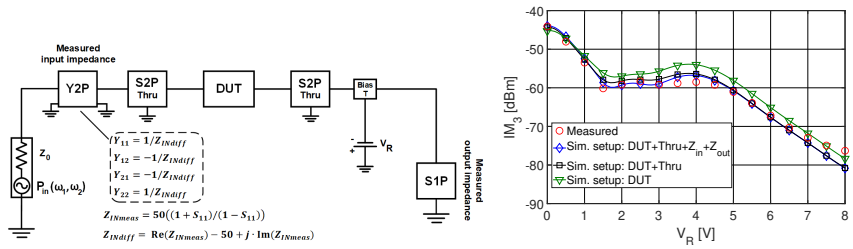

(a) **(b)**

Figure 4.12. (a) Illustration of the simulation setup in Paper C. The input is composed of the signal generator, the measured input impedance of the measurement setup as a Y2P component, and the S2P of the thru. The output is composed of the measured output impedance of the measurement setup as an S1P, the bias setup, and the S2P of the thru. The simulated system impedance $Z_0 = 50\ \Omega$. (b) Comparison of different simulation setups.

signal generators that are connected to a combiner, which is connected to the DUT. The IMD generated in the DUT is often measured with a spectrum analyzer. This type of measurement was carried out for the phase shifters in Paper A and Paper B. In Fig. 4.13, each signal generator is connected to a low-pass filter that is connected to an isolator. The low-pass filter suppresses any higher-order harmonics generated in the signal generators, and the isolator is there to avoid any leakage between the channels and suppress any reflections.

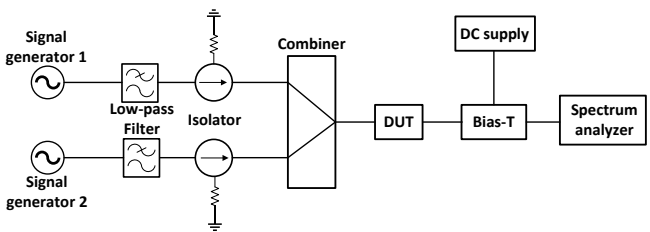

Figure 4.13. Illustration of a two-tone measurement setup employed in Paper A and Paper B.

In Paper C, a similar measurement setup was utilized with the difference that a Keysight PNA-X N5247B both generated the two fundamental signals and measured the intermodulation with the swept IMD measurement type enabled. Two sources generate the two fundamental signals internally of the PNA, and the two signals eject two different ports. The DUT is then connected

to a third PNA port that measures the generated IMD. An illustration of the measurement setup is provided in Fig. 4.14a, and the measurement setup is shown in Fig. 4.14b.

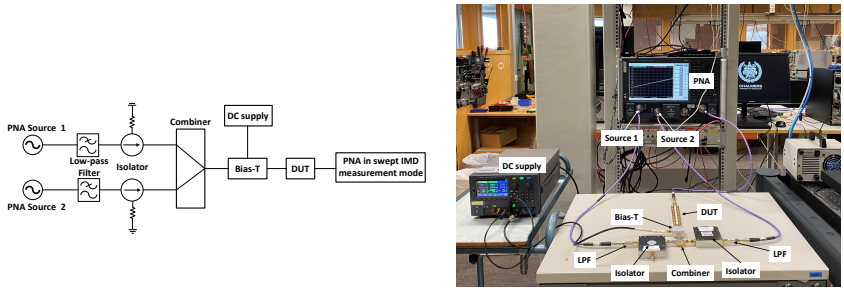

(a) **(b)**

Figure 4.14. (a) Illustration of the two-tone measurement setup for forward IM. The fundamental signals are generated by the PNA internally, and the IM is measured with the same PNA at a third port in swept IMD measurement mode. (b) The measurement setup.

Nonlinear results

In this chapter, it is emphasized that accurately acquiring the parasitic elements of the varactor model, specifically the inductance, and considering the impedance at the input and output of the DUT is crucial to modeling IMD accurately. By doing so, it simplifies the process of finding the correct model parameters and reduces uncertainty. For instance, Paper A and Paper B both used the same phase shifters, but the model in Paper B was further developed. The varactor model parameters were taken from the datasheet, and the coaxial connector was described as an LC-network. These parameters were optimized to fit the measured S-parameter results. Fig. 4.15 shows IM_3 for the phase shifter with 7 unit cells. While Paper A showed discrepancies, Paper B's results were greatly improved and described the nonlinear behavior well, particularly at low input powers. The method demonstrated good results, but the varactor model parameters' accuracy cannot be guaranteed since the optimization might yield incorrect values, and the LC-network might also impact the varactor model parameters. The more reliable approach is to follow the process in Paper C, where the behavior of the thru line connecting to the DUT is known, and the parasitics are determined from measurement. This approach makes the model more reliable, and no optimization is necessary.

In Paper A, we analyzed the simulated forward and backward IM_3 products

in 1 to 11 unit cells for a bias of -0.5 V, and the results are depicted in Fig. 4.16. As we increase the number of unit cells, the forward IMD increases. On the other hand, the behavior of the backward IM_3 depends on whether the phase shifter has an odd or even number of unit cells. Higher odd numbers of unit cells result in lower IM_3 values. For example, the IM_3 for 11 unit cells is lower than that for a single unit cell. This observation can be explained by destructive interference, as explained in [10]. When two nonlinear sites are separated by an odd number of quarter wavelengths, the IM_3 value is minimized due to destructive interference. Conversely, when an even number of quarter wavelengths are present between the sites, a maximum of IM_3 is obtained. Hence, the lower IM_3 value in 11 unit cells can be attributed to the destructive interference of the multiple IM sources.

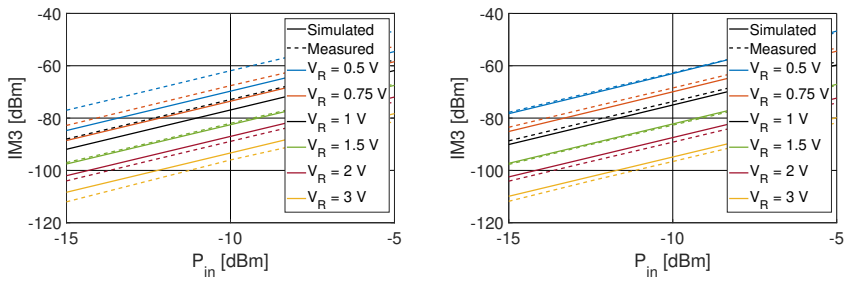

Figure 4.15. The IM_3 for the phase shifter with 7 unit cells with the model employed in (a) Paper A and (b) Paper B.

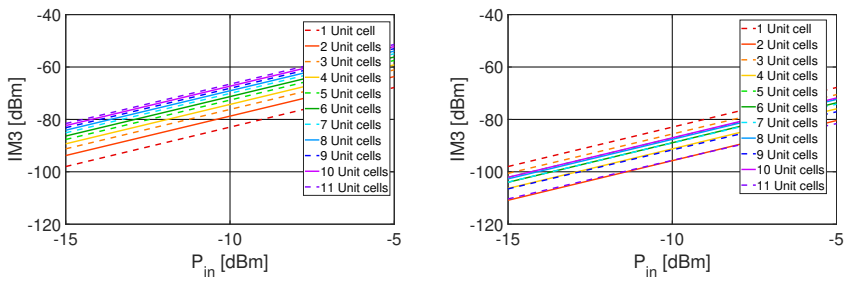

Figure 4.16. Simulated IM_3 for different numbers of T-unit cells in Paper A. (a) Forward IM_3. (b) Backward IM_3.

Fig. 4.17 depicts the simulated and measured IM_3 for the phase shifters with a unit cell length of 57.7° in Paper C. For the phase shifters with the uniform Schottky varactor-diode, the IM_3 increases when V_R moves towards 0 V. This is not the case for the highly nonuniform hyberabrupt varactor-diode and, therefore, the IM_3 is presented as a function of V_R for a fixed input power of 1.6 dBm in Fig. 4.17. For a single unit cell, the IM_3 initially peaks at 0 V and then gradually decreases until it becomes relatively constant between 1.5 V and 4 V and decreases further as V_R increases beyond 4 V. In contrast, the phase shifters with 5 and 10 unit cells exhibit IM_3 cancellation effects at zero volts, and then reach a maximum around 1 V. The IM_3 then fluctuates between 1 V and 4 V, creating local minima and maxima. After 4 V, the IM_3 decreases again with increasing V_R. The IM_3 increases with increasing input power with a slope of 3 dB/dB, like the result shown in Fig. 4.15. Therefore, is the shape of the IM_3 in Fig. 4.17 identical for a different input power.

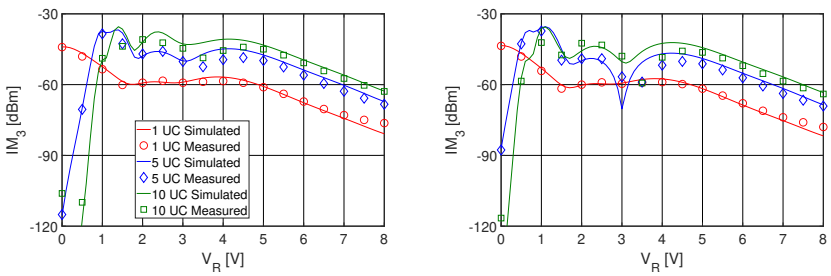

Figure 4.17. IM_3 for the phase shifter with a unit cell length of 57.7° in Paper C for (a) upper-band (b) lower-band.

Lastly, the IM_3 results with the model of C_j in (4.2) are shown in Fig. 4.18. The figure shows that (4.2) cannot accurately model the nonlinear behavior for the highly nonuniform hyberabrupt varactor-diode. This demonstrates that the C-V characteristics must be carefully modeled to describe the nonlinear behavior.

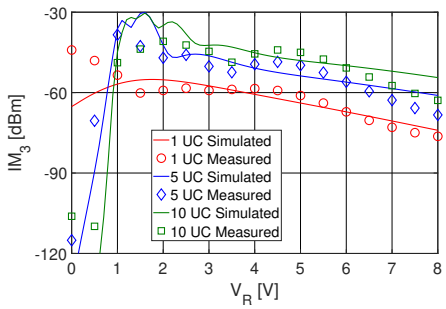

Figure 4.18. Measured and simulated IM_3 when the model in (4.2) is employed.

CHAPTER 5

Optimum design of loaded-line phase shifters

In the previous chapter, a model of the hyperabrupt varactor-diode was presented. It will be utilized in this chapter to investigate whether there is an optimum design of loaded-line phase shifters with respect to both FOM and linearity. The study is performed in a simulation that extends the range of parameter values to investigate. In Section 5.1, the influence of unit cell length is investigated, and in Section 5.2, the influence of the varactor-diodes quality factor is investigated. Finally, a conclusion of the study is presented in Section 5.3.

5.1 Influence of unit cell length

The study of influence of the unit cell length was performed with the phase shifter with an unit cell length of 57.7° from Paper C. Therefore, the parameters C_V, θ_0, R_s, and L_s refer to that unit cell. The study was performed by reducing the unit cell length of the reference unit cell. The effect of reducing the unit cell length is that the capacitance per unit cell length will increase, which is undesirable for the comparison. Instead, the capacitance per unit cell length should be consistent for all different unit cell lengths that were compared to have a fair comparison. This was achieved by modifying the varactor's capacitance with the same amount of reduction of the unit cell length. However, reducing C_V will also affect the quality factor of the varactor, and therefore, the series resistance had to be modified to compensate for the change in quality factor.

Fig. 5.1 illustrates how θ_0, C_V, and R_s are scaled with the value N. As we are reducing the length of the unit cell, θ_0 and C_V are divided by N, and R_s is multiplied by N. This enables a comparison where the unit cell length is different while the capacitance per unit cell length and the quality factor is maintained for each unit cell. In this study, N is chosen to have the value of 1, 2, 4, and 8, where $N = 1$ for the reference unit cell.

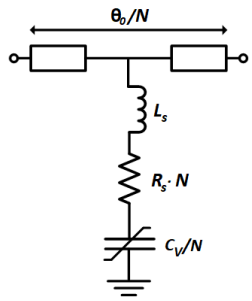

Figure 5.1. Modification of the unit cell to maintain the same capacitance per unit cell length and quality factor for all phase shifters. The reference unit cell has an $N = 1$.

As a starting point for comparison, the θ_e, IL, C_V and IM_3 for each unit cell is depicted in Fig. 5.2. It should be noted here, that when θ_0 is divided, θ_e is not reduced with the same amount as θ_0 due to the dispersive behavior of the unit cells. The comparison shows that the IL reduces with a reduced length. The C_V is scaled exactly with N as expected. The IM_3 is lowered at a larger revered bias ($V_R > 3.5$ V) with a shorter unit cell. At a lower reversed bias, the reference unit cell has an IM_3 similar to $\theta_0/2$ and $\theta_0/4$.

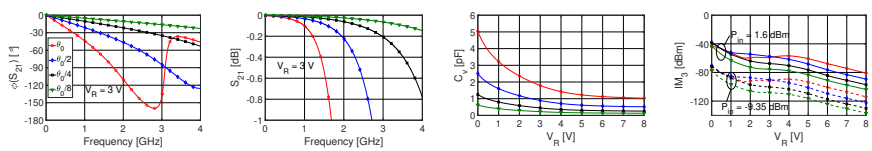

(a) **(b)** **(c)** **(d)**

Figure 5.2. For each unit cell, here is the (a) phase shift, (b) insertion loss, (c) varactor capacitance, and (d) third-order intermodulation presented.

The phase shift from a single unit cell is seldom sufficient for real applications. Therefore, the reference phase shifter was designed with 10 unit cells which gives a differential phase shift larger than 180°. The physical length was the

same between all phase shifters in the comparison. Therefore, had the phase shifters with unit cell lengths of $\theta_0/2$, $\theta_0/4$, and $\theta_0/8$, 20, 40, and 80 unit cells, respectively. The unit cells had different IL and it was suspected that they might have different tuning ranges that optimize their FOM. Therefore, the differential phase shift and the FOM were plotted as functions of V_{Rmin} when V_{Rmax} was set to 8 V, at the fundamental frequency of 1.5 GHz, as depicted in Fig. 5.3. If the tuning range is the same, one can conclude from the figure that the largest differential phase shift is generated for the phase shifter with the longest unit cell, and the greatest FOM is generated for the phase shifter with the shortest unit cell. However, with a shorter unit cell, the IL reduces and enables a larger tuning range with a larger FOM. Therefore, Fig. 5.3 was utilized to find the V_{Rmin} that generated the maximum FOM for each phase shifter. The figure shows that the phase shifters with a unit cell length of θ_0, $\theta_0/2$, $\theta_0/4$, and $\theta_0/8$, generates the largest FOM when V_{Rmin} is 3 V, 2.25 V, 2 V, and 1.75 V, respectively.

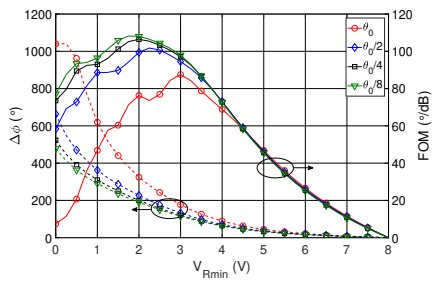

Figure 5.3. The differential phase and FOM when V_{Rmin} is varied and V_{Rmax} is set to 8 V, for each phase shifter with the different unit cell lengths of θ_0, $\theta_0/2$, $\theta_0/4$, and $\theta_0/8$. The plot shows which V_{Rmin} generates the largest FOM for each phase shifter when $V_{\mathrm{Rmax}} = 8$ V.

The differential phase shift and FOM was then studied versus frequency in Fig. 5.4 when V_{Rmin} is selected to maximize FOM for each phase shifter. The phase shifter with the shortest unit cell has the greatest FOM over the majority of the frequency spectrum and the largest differential phase shift from DC to 1.7 GHz. However, it should be noted that both FOM and $\Delta\phi$ are quite similar for all phase shifters with reduced unit cell length from DC to 1.7 GHz. The upper-band IM_3 versus V_R is depicted in Fig. 5.5 to evaluate the linearity of the phase shifters. In the lower region of V_R, the IM_3 is the smallest for the phase shifter with a unit cell length of θ_0, and the largest IM_3 is found for the phase shifter with a unit cell length of $\theta_0/8$. At a V_R above 4.4 V, the reference phase shifter obtains the largest IM_3.

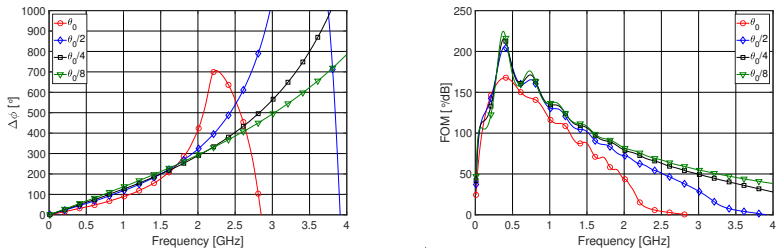

(a) (b)

Figure 5.4. (a) Differential phase and (b) FOM when V_{Rmin} is selected to generate maximum FOM for each phase shifter with the different unit cell lengths of θ_0, $\theta_0/2$, $\theta_0/4$, and $\theta_0/8$.

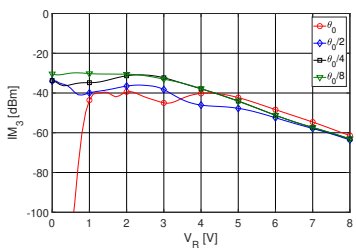

Figure 5.5. Upper-band IM_3 at $P_{\mathrm{in}} = 1.6$ dBm for each phase shifter with the different unit cell lengths of θ_0, $\theta_0/2$, $\theta_0/4$, and $\theta_0/8$.

The results show that having a shorter unit cell improves the phase shifter performance. In the case of linearity, a longer unit cell can reduce the IM_3. However, in this case, the reference phase shifter cannot utilize its linearity in the lower region of V_R due to the large IL in that region. Therefore, it is a trade-off between phase shifter performance and linearity. It could be argued that the phase shifter with a unit cell of length $\theta_0/2$ gives the best the trade-off between the FOM and linearity as it has similar FOM as the phase shifter with the shortest unit cell, and have the best linearity compared to the phase shifters with reduced unit cell length.

5.2 Influence of varactor-diode quality factor

The same reference unit cell is employed in this study as the previous section. The quality factor of the reference unit cell is denoted as Q_0, and the quality

factor was modified by changing R_s in the varactor-diode model. Five phase shifters were compared and the quality factor of their varactor-diodes are $4Q_0$, $2Q_0$, Q_0, $Q_0/2$, and $Q_0/4$, which corresponds to the series resistance of $R_s/4$, $R_s/2$, R_s, $2R_s$, and $4R_s$, respectively. Fig. 5.6 depicts the quality factor for each varactor-diode at 1.5 GHz.

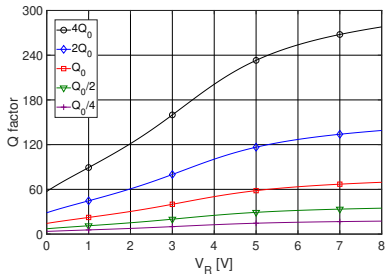

Figure 5.6. The quality factor at 1.5 GHz for the varactor-diodes employed in the phase shifters compared.

The number of unit cells are 10 for all phase shifters. The phase shifters have the same length and the quality factor affects θ_e marginally. Therefore, the differential phase shift is similar for all phase shifters except when they reach the cut-off region, as depicted in Fig. 5.7a. However, the quality factor affects the IL greatly as depicted in Fig. 5.7b. The IL is greatly improved with an increased quality factor and this results in an larger FOM, which is shown in Fig. 5.7c.

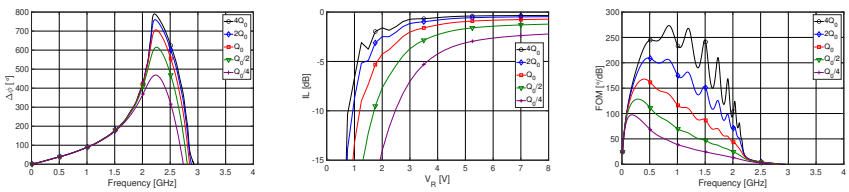

Figure 5.7. (a) Differential phase shift, (b) IL and (c) FOM for varying Q factors.

Fig. 5.8 shows the IM_3 for the five phase shifters, the result shows that a larger quality factor increases the IM_3. The increased IM_3 is the result of the smaller series resistance. When R_s is reduced, the voltage swing over R_s is smaller and the voltage swing over C_V increases, which in turn increases the IM distortion. From the results, one can see that a larger quality factor

improves the phase shifter performance greatly. However, it should be noted that there is a trade-off between low loss and IMD.

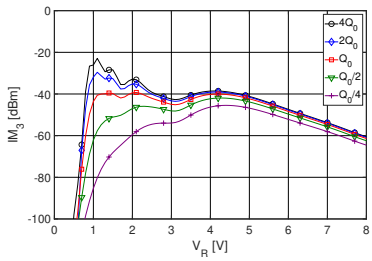

Figure 5.8. Upper-band IM_3 for varying Q factor at $P_{\text{in}} = 1.6$ dBm.

5.3 Conclusions of simulation study

In this chapter, it was investigated if there is an optimum design of loaded-line phase shifters with respect to FOM ($\Delta\phi_{\text{degree}}/L_{\text{dB}}$) and linearity. It was performed with a simulation study to further extend the range of model parameters that affect the FOM and linearity. The varactor-model and phase shifter in Paper C was employed in the study and utilized as a reference. First, the influence of the unit cell length was studied, where the capacitance per unit cell length and the quality factor is maintained for each unit cell. Secondly, the influence of the quality factor was investigated. The conclusions of the study are:

1. FOM is primarily dependent on Q factor and distribution of varactor capacitance. For the same varactor capacitance per unit length, it is generally advantageous to distribute the capacitance more evenly, i.e., increase the number of unit cells.

2. In terms of intermodulation distortion for given input power, it is primarily proportional to the total varactor capacitance per unit cell. However, there is also a dependency on the electric length of the unit cell. For electrically long cells, cancellation effects may reduce IMD in the regions where it is otherwise the highest.

3. There is a trade-off between low loss and low intermodulation. The higher the quality factor, the higher intermodulation for two otherwise similar phase shifters.

CHAPTER 6

Conclusions and future work

6.1 Conclusions

In this thesis, intermodulation distortion has been analyzed and modeled in loaded-line phase shifters periodically loaded by varactor-diodes. Several phase shifters were designed and realized, and two types of varactor-diodes were employed. These were a silicon Schottky and a silicon hyperabrupt varactor-diode. The IMD generated in loaded-line phase shifters has been investigated for several design factors, e.g., periodicity, bias condition, input power, number of unit cells, and capacitance per unit cell length.

For the phase shifters with the silicon Schottky varactor-diode, where the distance between two nonlinear sources was 90°, it was demonstrated that forward IMD increases when more unit cells are added. However, for backward IMD destructive interference generated lower IMD when an odd number of unit cells were employed. In the case of the phase shifters with the hyperabrupt varactor-diode, IM cancellation effects and local minima occurred for forward IMD depending on the applied reversed bias.

Two types of varactor models were investigated and compared for the hyperabrupt varactor-diode. The result demonstrated that the C-V characteristics and parasitics, especially the inductance, must be accurately modeled to describe the nonlinear behavior. Additionally, the extraction of the varactor model was described.

The model was employed to investigate if there is an optimum design with

respect to phase-shift/loss and linearity for the loaded-line phase shifter. The investigation was performed in a simulation setting to further extend the range of model parameters. It was demonstrated that the phase-shift/loss primarily depends on the Q factor and distribution of varactor capacitance. For the same varactor capacitance per unit length, the phase-shift/loss can be improved by distributing the capacitance more evenly. The IMD is primarily proportional to the total varactor capacitance per unit cell. It was also shown that there is a trade-off between low intermodulation and low loss, a higher quality factor results in higher IMD.

6.2 Future work

The future work in this project regards passive intermodulation generated in the feeding network of antennas utilized for satellite communication. The feed network has a surface treatment in the form of anodization, producing an oxidation layer that enhances heat dissipation in space. The oxidation layer contains certain irregularities, such as grain boundaries and dendrites, which may be the predominant source of PIM in the feeding networks. To better understand this issue, we will develop a model and compare it with measured results in order to identify the primary source of PIM in the feeding network.

References

[1] Ericsson AB, "Ericsson mobility report," Ericsson, Tech. Rep., 2022.

[2] I. Angelov, L. Bengtsson, and M. Garcia, "Extensions of the chalmers nonlinear HEMT and MESFET model," *IEEE Transactions on Microwave Theory and Techniques*, vol. 44, no. 10, pp. 1664–1674, 1996. DOI: 10.1109/22.538957.

[3] J. Cai, J. King, and J. C. Pedro, "A new nonlinear behavioral modeling technique for RF power transistors based on bayesian inference," in *2017 IEEE MTT-S International Microwave Symposium (IMS)*, 2017, pp. 624–626. DOI: 10.1109/MWSYM.2017.8058645.

[4] Y. YAMAMOTO and N. KUGA, "A short-circuit transmission line method for pim evaluation of metallic materials," in *2006 Asia-Pacific Microwave Conference*, 2006, pp. 1461–1464. DOI: 10.1109/APMC.2006.4429682.

[5] J. R. Wilkerson, K. G. Gard, A. G. Schuchinsky, and M. B. Steer, "Electro-thermal theory of intermodulation distortion in lossy microwave components," *IEEE Transactions on Microwave Theory and Techniques*, vol. 56, no. 12, pp. 2717–2725, 2008. DOI: 10.1109/TMTT.2008.2007084.

[6] C. Vicente and H. Hartnagel, "Passive-intermodulation analysis between rough rectangular waveguide flanges," *IEEE Transactions on Microwave Theory and Techniques*, vol. 53, no. 8, pp. 2515–2525, 2005. DOI: 10.1109/TMTT.2005.852771.

[7] D. E. Zelenchuk, A. P. Shitvov, A. G. Schuchinsky, and V. F. Fusco, "Passive intermodulation in finite lengths of printed microstrip lines," *IEEE Transactions on Microwave Theory and Techniques*, vol. 56, no. 11, pp. 2426–2434, 2008. DOI: 10.1109/TMTT.2008.2005886.

[8] C. Vicente, D. Wolk, H. L. Hartnagel, B. Gimeno, V. E. Boria, and D. Raboso, "Experimental analysis of passive intermodulation at waveguide flange bolted connections," *IEEE Transactions on Microwave Theory and Techniques*, vol. 55, no. 5, pp. 1018–1028, 2007. DOI: 10.1109/TMTT.2007.895400.

[9] J. Henrie, A. Christianson, and W. J. Chappell, "Prediction of passive intermodulation from coaxial connectors in microwave networks," *IEEE Transactions on Microwave Theory and Techniques*, vol. 56, no. 1, pp. 209–216, 2008. DOI: 10.1109/TMTT.2007.912166.

[10] J. R. Wilkerson, P. G. Lam, K. G. Gard, and M. B. Steer, "Distributed passive intermodulation distortion on transmission lines," *IEEE Transactions on Microwave Theory and Techniques*, vol. 59, no. 5, pp. 1190–1205, 2011. DOI: 10.1109/TMTT.2011.2106138.

[11] D. S. Kozlov, A. P. Shitvov, A. G. Schuchinsky, and M. B. Steer, "Passive intermodulation of analog and digital signals on transmission lines with distributed nonlinearities: Modelling and characterization," *IEEE Transactions on Microwave Theory and Techniques*, vol. 64, no. 5, pp. 1383–1395, 2016. DOI: 10.1109/TMTT.2016.2550046.

[12] P. Bolli, S. Selleri, and G. Pelosi, "Passive intermodulation on large reflector antennas," *IEEE Antennas and Propagation Magazine*, vol. 44, no. 5, pp. 13–20, 2002. DOI: 10.1109/MAP.2002.1077773.

[13] D. Smacchia, P. Soto, V. E. Boria, *et al.*, "Advanced compact setups for passive intermodulation measurements of satellite hardware," *IEEE Transactions on Microwave Theory and Techniques*, vol. 66, no. 2, pp. 700–710, 2018. DOI: 10.1109/TMTT.2017.2783383.

[14] D. S. Kozlov, A. P. Shitvov, and A. G. Schuchinsky, "Passive intermodulation in distributed circuits with cascaded discrete nonlinearities," in *2015 9th European Conference on Antennas and Propagation (EuCAP)*, 2015, pp. 1–5.

[15] Q. Jin, J. Gao, G. T. Flowers, Y. Wu, and G. Xie, "Modeling of passive intermodulation with electrical contacts in coaxial connectors," *IEEE Transactions on Microwave Theory and Techniques*, vol. 66, no. 9, pp. 4007–4016, 2018. DOI: 10.1109/TMTT.2018.2838147.

[16] X. Chen, Y. He, S. Yang, *et al.*, "Analytic passive intermodulation behavior on the coaxial connector using monte carlo approximation," *IEEE Transactions on Electromagnetic Compatibility*, vol. 60, no. 5, pp. 1207–1214, 2018. DOI: 10.1109/TEMC.2018.2809449.

[17] H. Yang, H. Wen, Y. Qi, and J. Fan, "An equivalent circuit model to analyze passive intermodulation of loose contact coaxial connectors," *IEEE Transactions on Electromagnetic Compatibility*, vol. 60, no. 5, pp. 1180–1189, 2018. DOI: 10.1109/TEMC.2018.2794992.

[18] X. Zhao, Y. He, M. Ye, *et al.*, "Analytic passive intermodulation model for flange connection based on metallic contact nonlinearity approximation," *IEEE Transactions on Microwave Theory and Techniques*, vol. 65, no. 7, pp. 2279–2287, 2017. DOI: 10.1109/TMTT.2017.2668402.

[19] C. Ge, B. Duan, W. Wang, S. Qian, and S. Lou, "An equivalent circuit model for rectangular waveguide performance analysis considering rough flanges' contact," *IEEE Transactions on Microwave Theory and Techniques*, vol. 67, no. 4, pp. 1336–1345, 2019. DOI: 10.1109/TMTT.2019.2896556.

[20] Y. R. Mao, Y. Liu, Y. J. Xie, and Z. H. Tian, "Simulation of electromagnetic performance on mesh reflector antennas: Three-dimensional mesh structures with lumped boundary conditions," *IEEE Transactions on Antennas and Propagation*, vol. 63, no. 10, pp. 4599–4603, 2015. DOI: 10.1109/TAP.2015.2459133.

[21] Y. Liu, Y. R. Mao, Y. J. Xie, and Z. H. Tian, "Evaluation of passive intermodulation using full-wave frequency-domain method with nonlinear circuit model," *IEEE Transactions on Vehicular Technology*, vol. 65, no. 7, pp. 5754–5757, 2016. DOI: 10.1109/TVT.2015.2483738.

[22] D. Wu, Y. Xie, Y. Kuang, and L. Niu, "Prediction of passive intermodulation on mesh reflector antenna using collaborative simulation: Multiscale equivalent method and nonlinear model," *IEEE Transactions on Antennas and Propagation*, vol. 66, no. 3, pp. 1516–1521, 2018. DOI: 10.1109/TAP.2017.2786304.

[23] J. A. Greenwood, J. B. P. Williamson, and F. P. Bowden, "Contact of nominally flat surfaces," *Proceedings of the Royal Society of London. Series A. Mathematical and Physical Sciences*, vol. 295, no. 1442, pp. 300–319, 1966. DOI: 10.1098/rspa.1966.0242.

[24] L. Kogut and I. Etsion, "A finite element based elastic-plastic model for the contact of rough surfaces," *Tribology Transactions*, vol. 46, no. 3, pp. 383–390, 2003. DOI: 10.1080/10402000308982641.

[25] J. G. Simmons, "Generalized formula for the electric tunnel effect between similar electrodes separated by a thin insulating film," *Journal of Applied Physics*, vol. 34, pp. 1793–1803, 1963.

[26] J. Russer, A. Ramachandran, A. Cangellaris, and P. Russer, "Phenomenological modeling of passive intermodulation (PIM) due to electron tunneling at metallic contacts," in *2006 IEEE MTT-S International Microwave Symposium Digest*, 2006, pp. 1129–1132. DOI: 10.1109/MWSYM.2006.249389.

[27] J. R. Wilkerson, K. G. Gard, and M. B. Steer, "Electro-thermal passive intermodulation distortion in microwave attenuators," in *2006 European Microwave Conference*, 2006, pp. 157–160. DOI: 10.1109/EUMC.2006.281242.

[28] T. Bechtold, E. B. Rudnyi, and J. G. Korvink, "Dynamic electro-thermal simulation of microsystems—a review," *Journal of Micromechanics and Microengineering*, vol. 15, no. 11, R17, Oct. 2005. DOI: 10.1088/0960-1317/15/11/R01.

[29] J. Pedro and N. Carvalho, *Intermodulation Distortion in Microwave and Wireless Circuits*. Artech House, 2003.

[30] K. Mayaram, D. Lee, S. Moinian, D. Rich, and J. Roychowdhury, "Computer-aided circuit analysis tools for RFIC simulation: Algorithms, features, and limitations," *IEEE Transactions on Circuits and Systems II: Analog and Digital Signal Processing*, vol. 47, no. 4, pp. 274–286, 2000. DOI: 10.1109/82.839663.

[31] K. Kundert, G. Sorkin, and A. Sangiovanni-Vincentelli, "Applying harmonic balance to almost-periodic circuits," *IEEE Transactions on Microwave Theory and Techniques*, vol. 36, no. 2, pp. 366–378, 1988. DOI: 10.1109/22.3525.

[32] M. Nakhla and J. Vlach, "A piecewise harmonic balance technique for determination of periodic response of nonlinear systems," *IEEE Transactions on Circuits and Systems*, vol. 23, no. 2, pp. 85–91, 1976. DOI: 10.1109/TCS.1976.1084181.

[33] K. Kundert, "Introduction to RF simulation and its application," *IEEE Journal of Solid-State Circuits*, vol. 34, no. 9, pp. 1298–1319, 1999. DOI: 10.1109/4.782091.

[34] P. Wambacq and W. Sansen, *Distortion Analysis of Analog Integrated Circuits*. The Netherlands, Dordrecht:Kluwer, 1998.

[35] R. E. Collin, *Foundations for Microwave Engineering, 2nd Edition*. New York: IEEE Press, Hoboken, N.J, 2001.

[36] R.M. Phillips, "The Ubitron, a high-power traveling-wave tube based on a periodic beam interaction in unloaded waveguide," *IRE Transactions on Electron Devices*, vol. 7, no. 4, pp. 231–241, 1960. DOI: 10.1109/T-ED.1960.14687.

[37] A. Nagra and R. York, "Distributed analog phase shifters with low insertion loss," *IEEE Transactions on Microwave Theory and Techniques*, vol. 47, no. 9, pp. 1705–1711, 1999. DOI: 10.1109/22.788612.

[38] D. Sievenpiper, J. Schaffner, H. Song, R. Loo, and G. Tangonan, "Two-dimensional beam steering using an electrically tunable impedance surface," *IEEE Transactions on Antennas and Propagation*, vol. 51, no. 10, pp. 2713–2722, 2003. DOI: 10.1109/TAP.2003.817558.

[39] C.-S. Lin, S.-F. Chang, C.-C. Chang, and Y.-H. Shu, "Design of a reflection-type phase shifter with wide relative phase shift and constant insertion loss," *IEEE Transactions on microwave theory and techniques*, vol. 55, no. 9, pp. 1862–1868, 2007.

[40] C.-S. Lin, S.-F. Chang, and W.-C. Hsiao, "A full-360° reflection-type phase shifter with constant insertion loss," *IEEE microwave and wireless components letters*, vol. 18, no. 2, pp. 106–108, 2008.

[41] K. Miyaguchi, M. Hieda, K. Nakahara, *et al.*, "An ultra-broad-band reflection-type phase-shifter MMIC with series and parallel LC circuits," *IEEE Transactions on Microwave Theory and Techniques*, vol. 49, no. 12, pp. 2446–2452, 2001.

[42] H. A. Atwater, "Circuit design of the loaded-line phase shifter," *IEEE Transactions on Microwave Theory and Techniques*, vol. 33, no. 7, pp. 626–634, 1985.

[43] H.-C. Chiu, C.-M. Chen, L.-C. Chang, and H.-L. Kao, "A 5-bit X-band GaN HEMT-based phase shifter," *Electronics*, vol. 10, no. 6, p. 658, 2021.

[44] D. Kuylenstierna, A. Vorobiev, P. Linner, and S. Gevorgian, "Composite right/left handed transmission line phase shifter using ferroelectric varactors," *IEEE Microwave and Wireless Components Letters*, vol. 16, no. 4, pp. 167–169, 2006. DOI: 10.1109/LMWC.2006.872145.

[45] D. Kuylenstierna, A. Vorobiev, P. Linner, and S. Gevorgian, "Ultrawideband tunable true-time delay lines using ferroelectric varactors," *IEEE Transactions on Microwave Theory and Techniques*, vol. 53, no. 6, pp. 2164–2170, 2005. DOI: 10.1109/TMTT.2005.848805.

[46] M. Rodwell, M. Kamegawa, R. Yu, M. Case, E. Carman, and K. Giboney, "GaAs nonlinear transmission lines for picosecond pulse generation and millimeter-wave sampling," *IEEE Transactions on Microwave Theory and Techniques*, vol. 39, no. 7, pp. 1194–1204, 1991. DOI: 10.1109/22.85387.

[47] S. A. Maas, *Nonlinear Microwave Circuits*. Norwood, MA: Artech House, 1988.

[48] G. Engen and C. Hoer, "Thru-reflect-line: An improved technique for calibrating the dual six-port automatic network analyzer," *IEEE Transactions on Microwave Theory and Techniques*, vol. 27, no. 12, pp. 987–993, 1979. DOI: 10.1109/TMTT.1979.1129778.